



## **Strain-age cracking of a $\gamma'$ -strengthened nickel-based superalloy additively manufactured by laser powder bed fusion**

Downloaded from: <https://research.chalmers.se>, 2026-06-08 05:11 UTC

Citation for the original published paper (version of record):

Xu, J., Shaikh, A., Boyle, H. et al (2026). Strain-age cracking of a  $\gamma'$ -strengthened nickel-based superalloy additively manufactured by laser powder bed fusion. *Acta Materialia*, 312. <http://dx.doi.org/10.1016/j.actamat.2026.122244>

N.B. When citing this work, cite the original published paper.



Full length article

# Strain-age cracking of a $\gamma'$ -strengthened nickel-based superalloy additively manufactured by laser powder bed fusion

Jinghao Xu<sup>a,\*</sup>, Abdul Shaafi Shaikh<sup>b,c</sup>, Henry Boyle<sup>a</sup>, Sofia Kazi<sup>b</sup>, Justinas Palisaitis<sup>d</sup>, Ru Lin Peng<sup>a</sup>, Eduard Hryha<sup>b</sup>, Johan Moverare<sup>a</sup>

<sup>a</sup> Division of Engineering Materials, Linköping University, 58183, Linköping, Sweden

<sup>b</sup> Department of Industrial and Materials Science, Chalmers University of Technology, Rännvägen 2A, 41296, Gothenburg, Sweden

<sup>c</sup> Electro Optical Systems Finland Oy, Lemminkäisenkatu 36, 20520 Turku, Finland

<sup>d</sup> Thin Film Physics Division, Department of Physics, Chemistry and Biology (IFM), Linköping University, 58183, Linköping, Sweden

## ARTICLE INFO

## Keywords:

Nickel-based superalloy  
Laser powder bed fusion  
Additive manufacturing  
Strain-age cracking  
Residual stress

## ABSTRACT

Strain-age cracking (SAC) remains a critical barrier in post-processing of  $\gamma'$ -strengthened nickel-based superalloys manufactured by laser powder bed fusion (PBF-LB). In this work, the SAC susceptibility of PBF-LB IN738LC was systematically investigated using V-notch samples under different heating conditions. Residual strain evolution during build plate removal was tracked by strain gauges, and residual stress at different notch depths was measured using synchrotron X-ray diffraction. SAC onset was determined by direct current potential drop (DCPD) and *in situ* optical imaging, while crack propagation kinetics were quantified under controlled heating rates and isothermal exposures. Post-mortem characterization of SAC morphologies was performed using X-ray photoelectron spectroscopy, scanning and transmission electron microscopy, energy-dispersive X-ray spectroscopy, and electron backscatter diffraction. SAC initiation is governed by  $\gamma'$  precipitation kinetics, with onset temperatures following the  $\gamma'$  precipitation behavior. Faster heating delays SAC onset, while isothermal holds trigger cracking after sufficient incubation, with longer times at lower isothermal temperatures. Shallow notches concentrate tensile stresses and develop extensive SAC, whereas deeper notches remain largely crack-free due to stress relaxation, sometimes aided by pre-existing solidification cracks. SAC propagates mainly along grain boundaries, assisted by wedge-shaped oxide intrusions. Fast-heating cross-sections reveal that most stored energy is released prior to SAC initiation, indicating that SAC results from instability of local ductility deficit rather than stress relief. Early-stage nanoscale  $\gamma'$  formation drives rapid strengthening and localized ductility loss, leading to SAC. These findings provide mechanistic insights and processing guidelines for mitigating SAC in PBF-LB superalloys.

## 1. Introduction

Due to its high design flexibility for net-shaped components, laser powder bed fusion (PBF-LB) is a promising manufacturing technique for producing geometrically complex parts such as turbine blades with internal cooling channels from  $\gamma'$ -strengthened nickel-based superalloys. However, post-processing heat treatment of PBF-LB-manufactured high  $\gamma'$  fraction superalloys remains a significant challenge. During heat treatment,  $\gamma'$  precipitation strengthens the alloy but simultaneously reduces its ductility. Residual stress retained from fabrication, combined with those stresses introduced during precipitation, can lead to strain-age cracking (SAC) in a form of solid-state cracking [1]. SAC often

manifests as extensive, millimeter-scale macrocracking and represents a major obstacle to the reliable post-processing of PBF-LB components.

Another issue of  $\gamma'$ -strengthened nickel-based superalloys during PBF-LB process is their intrinsic high solidification cracking susceptibility. This has been addressed through both alloy design [2–4] and optimization of PBF-LB processing parameters [5,6]. Meanwhile, these alloys still remain highly susceptible to SAC. Historically, SAC was studied extensively in welding. In nickel-based superalloys, transient  $\gamma'$  precipitation within the intermediate temperature range (~600–1100 °C) reduces ductility, and cracking may occur during post-weld heat treatment. Cracks often initiate due to residual stress, grain growth, constitutional liquation in the heat-affected zone (HAZ), or at stress

\* Corresponding author.

E-mail address: [jinghao.xu@liu.se](mailto:jinghao.xu@liu.se) (J. Xu).

<https://doi.org/10.1016/j.actamat.2026.122244>

Received 24 November 2025; Received in revised form 19 March 2026; Accepted 14 April 2026

Available online 18 April 2026

1359-6454/© 2026 The Author(s). Published by Elsevier Inc. on behalf of Acta Materialia Inc. This is an open access article under the CC BY license (<http://creativecommons.org/licenses/by/4.0/>).

concentration sites near the weld toe. Two primary factors contributing to SAC are  $\gamma'$  precipitation during post-treatment and residual stress retained in the material.

In contrast to welding, the PBF-LB process introduces several important differences. First,  $\gamma'$  is typically absent in the as-built condition. This suppression of  $\gamma'$  precipitation has been confirmed in a range of alloys including ABD-900AM [7], Haynes 282 [8], MAD542 [9], and IN738 [10], based on scanning (SEM) and transmission electron microscopy (TEM) as well as synchrotron X-ray diffraction analysis. In alloys with inherently high  $\gamma'$  content, such as IN713LC [11] and CM247LC [12], nanoscale  $\gamma'$  is occasionally observed in interdendritic regions. Nevertheless, in as-welded IN738LC superalloy,  $\gamma'$  is typically present in near-equilibrium amounts within the fusion zone [13,14], whereas in as-PBF-LB processed counterparts,  $\gamma'$  is commonly absent [15–17]. This absence in the as-built state results in significantly accelerated  $\gamma'$  precipitation kinetics during subsequent heat treatment.

The second key difference is the presence of high residual stress in the as-built condition. Due to localized melting and extremely high cooling rates, reaching up to hundreds of thousands of K/s [18], PBF-LB introduces significant thermal gradients and large residual stresses that can exceed the elastic limit of precipitation-strengthened alloys. For instance, residual stress in as-cast CMSX-4 superalloy is typically below 70 MPa [19]. In contrast, values above 1100 MPa have been reported for PBF-LB CM247LC using hole-drilling and synchrotron X-ray diffraction [20,21]. For a rough comparison, hoop stresses of approximately 800 MPa were reported in as-welded IN718 turbine disks [22]. Another distinction is the relatively high defect content in PBF-LB builds. Defects such as solidification cracks and lack of fusion features alter the state of residual stress. For instance, CM247LC with more defects exhibits lower residual stress levels as measured by X-ray diffraction [23], with solidification cracking being particularly effective at reducing residual stress [24].

These differences complicate the direct application of welding-based SAC knowledge to PBF-LB components. Nonetheless, a few studies have begun to explore SAC behavior in these materials subjected to PBF-LB. Markanday et al. [25] investigated SAC in cruciform specimens of various superalloys subjected to 1100 °C for 2 h heat treatment. SAC propensity was assessed based on  $\gamma'$  precipitation-related changes, including volume expansion, elastic modulus evolution, and the resulting loss of grain boundary (GB) ductility at elevated temperatures. Using dog-bone-shaped specimens with a side notch, Dörries et al. [26] demonstrated a trilemma in  $\gamma'$ -strengthened superalloys of SAM superalloy and its derivatives: it is not possible to simultaneously achieve hot cracking resistance, SAC resistance, and optimal minor element balance (e.g., boron, carbon, and zirconium). Boswell et al. [32] subjected PBF-LB CM247LC superalloy to post-processing heat treatments at various temperatures and identified SAC as the dominant cracking mechanism above 750 °C. They attributed this to the growth of  $\gamma'$  and carbides along cell boundaries, which hindered the relief of residual stresses through grain boundary sliding and micro-cracking.

Building on these initial studies, the present work provides a systematic investigation of SAC. In this study, SAC behavior of a widely used PBF-LB superalloy IN738LC is investigated. V-notch samples were intentionally designed to promote and isolate SAC during post-processing heat treatment. Both furnace and induction heating were used to evaluate SAC behavior under varied thermal conditions. SAC onset temperatures were determined using direct current potential drop (DCPD) and *in situ* optical imaging. SAC growth rates and transverse strain development were tracked during induction heating. Residual stress evolution was assessed through strain gauges (SGs) and synchrotron X-ray diffraction. Post-mortem characterization provided insight into SAC morphology and the role of grain boundary oxidation in SAC formation.

## 2. Materials and methods

Pre-alloyed vacuum inert gas melted and gas atomized IN738LC superalloy powder was used as feedstock for the PBF-LB build. The chemical composition is listed in Table 1. Multiple V-notch samples were printed using an EOS M290 PBF-LB system with the identical 40  $\mu\text{m}$  layer thickness process parameters defined in the parameter set “IN738\_Core\_1.00”. The build plate (substrate) was of carbon steel corresponding to EN C45U (1.1730) and was kept at 80 °C during the build. PBF-LB processing was performed under Ar shielding gas. The V-notch was intentionally designed to generate geometry-induced stress concentration and to localize the region of interest for SAC initiation and propagation. All V-notch samples share identical overall dimensions with height = 10 mm and width = 12 mm. The sample thickness was fixed at 2 mm to approximate plane-stress conditions. For the notch, they have the same opening distance of 6 mm but different notch depth (d) of 1, 2, 3, 4, 5, 6, 7 mm, and hence varying opening angle at the base of the notch. A photograph of the prints and the schematic drawing of the V-notch samples are shown in Fig. 1.

### 2.1. Heat treatment

The heat treatment of nickel-based superalloys typically comprises two steps: solution treatment followed by aging, for chemical homogenization and  $\gamma'$  precipitation control. To date, no dedicated heat treatment scenario has been specifically developed for the PBF-LB processed IN738LC superalloy. Therefore, a solution treatment temperature of 1120 °C was selected, which was originally designed for cast IN738LC [27,28] and has since been widely adopted as a post-processing heat treatment temperature for PBF-LB IN738LC [29,30]. Two different heating environments were used for the heat treatments in this study. For the heat treatment at 1120 °C, a laboratory chamber furnace Rohde ME30 (Helmut Rohde GmbH, Prutting, Germany) was used. For the induction heating at various temperatures, a thermomechanical fatigue system equipped with an induction heating system TruHeat HF 3010 (TRUMPF Hüttinger GmbH + Co. KG, Freiburg im Breisgau, Germany) was used. A grooved bar made of Sanicro25 alloy was used to hold the V-notch sample. Two type-K thermocouples were spot-welded to opposite sides of the V-notch sample: one for temperature control and the other for monitoring using a Pico data logger TC-08 (Pico Technology Ltd, Cambridgeshire, UK). The average value of the controlling and monitoring thermocouples represents the sample temperature. Heating rates varied from nominal rates of 8–1200 °C/min. All the heat treatments in this study were carried out in ambient air.

The *in situ* observations of geometrical changes close to notches were made during the induction heating tests via a microscope camera (USB29 QXC F) with a maximum resolution of 2592  $\times$  1944 pixels. The pixel-to-length scale was calibrated based on the width of the V-notch samples, resulting in a pixel resolution of approximately 5.2  $\mu\text{m}/\text{pixel}$ . A constant exposure time of 400 ms was selected for testing at slow heating rate (8 °C/min) and isothermal conditions, 100 ms and 50 ms were used for fast heating rate conditions for the camera. Open-source software Fiji [31] was used for post image-analysis.

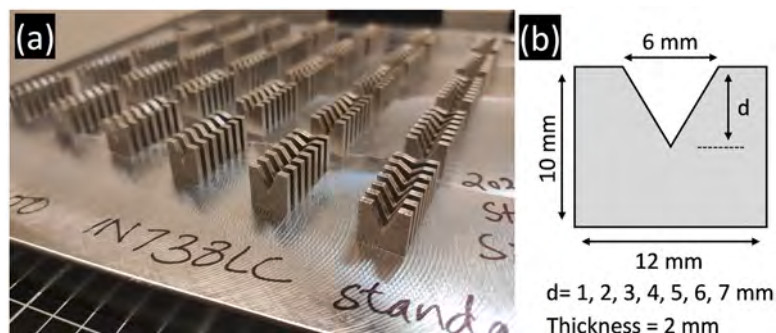
### 2.2. Strain measurement during EDM

Strain was measured using linear strain gauges (1-LY51–3/120, HBK, Darmstadt, Germany) bonded with CA80 adhesive (HBK, Darmstadt, Germany) to the wall surface of the V-notch sample to capture the transverse strain perpendicular to the building direction during the sample cutting. To protect the SGs, a water-proof capsule was carefully made with X60 cold curing glue (HBK, Darmstadt, Germany). Two quarter bridge circuits were used for the SGs. The data acquisition was carried out on a SG amplifier (QuantumX MX1615B) with a logging rate of 5 Hz. The excitation voltage was 2.0 V. During electrical discharge machining (EDM) wire cutting, a constant speed of 3.6 mm/min was

**Table 1**

Chemical composition of IN738LC powder used for manufacturing of samples in wt. %.

Ni	Cr	Co	Al	Ti	Mo	W	Ta	Nb	Si	S	Zr	B	C
Bal.	15.9	8.9	3.24	3.65	1.85	2.76	1.61	1.04	0.037	0.002	0.027	0.013	0.10

**Fig. 1.** (a) Photo of the printed IN738LC V-notch samples on build plate, and (b) the schematic drawing of the V-notch sample.

used while recording SG data.

### 2.3. DCPD measurement

A direct current potential drop measurement was used in this study to measure SAC onset during furnace heat treatment of the V-notch samples. DCPD is widely used for measuring the crack growth rate during mechanical testing [32]. A direct current of 1 A was applied by a TSX1820 precision DC power supply unit (Aim-TTi, Cambridgeshire, United Kingdom). For temperature measurement on the sample, a type-K thermocouple was spot-welded directly on the surface of the sample.

### 2.4. Residual stress measurement

Residual stress measurements were carried out using the synchrotron X-ray transmission diffraction method at P07 HEMS beamline of PETRA III, DESY. A monochromatic X-ray beam (73.3 keV) was transmitted through the sample, and the diffracted beams were collected by a 2D detector positioned 2031 mm downstream. The defined beam size is 0.5 mm × 0.5 mm. The sample was moved stepwise along the building direction (BD) to measure positions at different distances from the notch tip. The first measurement was made once the Debye-Scherrer rings were clearly visible; this position was then denoted as being 0.25 mm from the notch tip. In the analytical procedure, we included the measurements only when the beam was fully in but not blocked by other materials. This was determined by examining the concentrated transmitted-beam footprint (direct-beam region) on the 2D detector (see Fig. A1 in the Appendix).

### 2.5. XPS analysis

X-ray photoelectron spectroscopy (XPS) was performed on SAC-fractured samples that underwent the full heat-treatment cycle at 1120 °C for 2 h, using a PHI 5000 system equipped with a monochromated Al K $\alpha$  source (1486.6 eV), with analysis conducted on fracture-surface regions corresponding to different SAC propagation stages for depth-resolved chemical characterization. Both survey scans and depth profiling were conducted at pass energies of 224 eV and 26 eV, respectively. Depth profiling was carried out by Ar<sup>+</sup> ion etching to a depth of approximately 300 nm, with the etch rate calibrated using a Ta<sub>2</sub>O<sub>5</sub> foil of known oxide thickness. Data was processed using PHI MultiPak software. Due to the instrument's minimum raster size of 1.0 mm × 1.0 mm, isolating the narrow "brown" transition region (between

the SAC and mechanical fracture surfaces) was not feasible. Survey spectra were acquired from 0.1 mm × 0.1 mm areas, while depth-profiling spectra were obtained only from the "light" (mechanical fracture) and "dark" (SAC) regions.

### 2.6. Microstructural characterization

Optical microscopy was used to characterize the as-built microstructure using a Leica DM6 Optical Microscope (Leica Microsystems GmbH, Wetzlar, Germany). A Leica M205C stereo microscope (Leica Microsystems GmbH, Wetzlar, Germany) was used to visualize the overall morphology of SAC and SG attachments on V-notch samples.

To characterize the fractography of SAC, cracked samples were mechanically forced open using an Instron 5582 testing system under manual control. The SAC fractures were carbon coated via a Leica EM ACE200 coating system (Leica Microsystems GmbH, Wetzlar, Germany). Secondary electron imaging was used to reveal the detailed SAC morphology using a Jeol JSM-IT500 scanning electron microscope (SEM). Another SEM (HITACHI SU-70) equipped with energy-dispersive X-ray spectroscopy (EDS) and electron backscatter diffraction (EBSD) was used for high-magnification cross-sectional characterization, with regions selected from crack-affected and adjacent matrix areas for elemental distribution mapping and crystallographic orientation analysis.

Metallographic sample preparation was carried out using a Struers Tegramin grinding and polishing machine (Struers ApS, Ballerup, Denmark) with Struers OP-U colloidal silica suspension finish. To enhance the visibility of different phases, etching was performed using Marble's reagent to dissolve  $\gamma$  by immersion of the polished samples for 10–15 s.

Focused ion beam (FIB) was employed to prepare TEM thin-foil lamellae by the conventional lift-out technique using a Thermo Scientific Helios 5 UC DualBeam system. The TEM lamellae were extracted along a plane generally perpendicular to the BD. TEM and high-resolution TEM (HRTEM) imaging and selective area electron diffraction (SAED) analyses were performed using an FEI Tecnai G2 microscope operated at an accelerating voltage of 200 kV.

## 3. Results

### 3.1. Original microstructure

The original microstructure of the V-notch samples in the as-built condition is characterized by stitched optical micrographs and

representative inverse pole figure (IPF) coloring maps with reference axis parallel to BD of  $d = 1$  mm and  $d = 7$  mm samples, as shown in Fig. 2. IN738LC is a well-known  $\gamma'$ -strengthened nickel-based superalloy with high susceptibility to microcracking during PBF-LB processing. To investigate the intrinsic SAC behavior during heat treatment, it is necessary to begin with material in the as-built condition containing minimal pre-existing cracks. Despite its cracking susceptibility, several studies have reported that IN738LC can be produced with largely crack-free microstructures under optimized PBF-LB processing conditions [33–36]. In this study, the samples were produced using optimized printing parameters, resulting in minimal metallurgical defects typical of PBF-LB, such as solidification cracks and lack of fusion. This is confirmed by the optical micrographs, which demonstrate the overall high printing quality.

As shown in the IPF maps superimposed with high-angle grain boundary plots, most grains exhibit a [001] orientation aligned with the BD. A clear distinction between the skin layer and the bulk material is visible, based on differences in grain orientation and morphology. Due to the use of specific skin layer (contour and upskin), grains near the surface display more random orientations. In contrast, the bulk region is characterized by highly columnar grains, whereas the surface region contains shorter and wider grains, resulting in a lower projected GB density along the BD.

### 3.2. Effect of removing from build plate

Fig. 3 illustrates the SAC behavior of V-notch samples heat-treated at  $1120^\circ\text{C}$  for 2 h in ambient air. This temperature is commonly used as the solutioning treatment for the IN738LC superalloy. Two sample configurations were investigated: (1) samples removed from the build plate prior to heat treatment, denoted as “off-plate,” and (2) samples heat-treated while still attached to a sliced section of the build plate, referred to as “on-plate.” As shown in Fig. 3(a), a stereo optical micrograph of mechanically opened off-plate samples reveals SAC cracks of varying lengths depending on notch depth. SAC length increases progressively with decreasing notch depth. This trend is quantitatively shown in Fig. 3(b), where SAC length is plotted against notch depth for both off-plate and on-plate samples. Off-plate samples generally exhibit slightly shorter SAC cracks than their on-plate counterparts, especially for deeper notches. For shallow notches (e.g.,  $d = 1$  mm), SAC lengths typically range from 3–5 mm, whereas SAC is absent in off-plate samples with notch depths greater than 5 mm and in on-plate samples beyond 6 mm. An exception is observed in a  $d = 1$  mm off-plate sample that did not exhibit SAC after heat treatment. As shown in Fig. 3(c), a stitched SEM micrograph of this sample reveals long pre-existing solidification

cracks near the notch tip. This observation suggests that the presence of solidification cracking prior to heat treatment may have locally relieved stresses, thereby suppressing the SAC formation in this sample.

Clearly, removal from the build plate reduces SAC propensity, but only to a limited extent. To understand this effect, it is essential to compare the evolution of residual stress, specifically the stress driving SAC opening, before and after removal. Fig. 4 presents transverse strain measurements obtained during the EDM cutting of V-notch samples off the build plate. Linear SGs were attached in the transverse direction (TD) at various heights from the build plate on different V-notch samples. Fig. 4(a) shows a photo of a SG attached sample prepared for EDM, and Fig. 4(b) displays stereo optical micrographs indicating SG placement.

Strain gauge readings recorded during EDM cutting are plotted in Fig. 4(c). Before immersion into the EDM coolant, the SG readings were reset to  $0\ \mu\epsilon$ . The compressive strain recorded after EDM cutting then reflects the release of tensile strain along the gauge direction. The deviation caused by coolant temperature is negligible compared to the total strain values, as seen in the stabilization stage. During EDM processing, a substantial drop in SG readings indicates significant release of transverse residual strain. However, the SG signal during this period is affected by multiple factors like electrical interference from EDM and should not be interpreted quantitatively. Therefore, residual strain values are taken at 600 s thus approximately 130 s after full detachment, when the signals were stabilized again.

The results reveal a clear trend: the released strain decreases with increasing height from the build plate. For example,  $1670\ \mu\epsilon$  was released at a height of 3.2 mm, while only  $531\ \mu\epsilon$  was released at 8.8 mm, corresponding to 125 MPa of tensile stress taken elastic modulus of 235 GPa (averaging from Ref. [10,17,37,38]) at room temperature of PBF-LB IN738LC superalloy along the direction perpendicular to BD. This confirms that the residual stresses along TD are strongly build height dependent. In the context of shallow notches, which are located higher above the build plate, less stress is released during removal, leaving significant tensile stress. Therefore, the limited mitigation of SAC observed in Fig. 3, especially in shallow notches, can be attributed to insufficient release of transverse residual stress during removal.

Residual stress measurements of off-plate V-notch samples in the as-built state were performed using synchrotron X-ray transmission diffraction. The experimental setup is illustrated in Fig. 5(a). Strains along the TD and BD were determined from the 311 lattice spacing ( $d^{311}$ ) extracted from 1D intensity profiles integrated over a narrow azimuthal sector ( $175^\circ$  to  $180^\circ$ ) and ( $265^\circ$  to  $270^\circ$ ) of the Debye-Scherrer ring, respectively [39,40]. The 1D profiles were fitted within the  $d$ -spacing range of  $1.064\ \text{\AA}$  to  $1.112\ \text{\AA}$  (corresponding to a  $2\theta$  range of  $8.7^\circ$  to  $9.1^\circ$ )

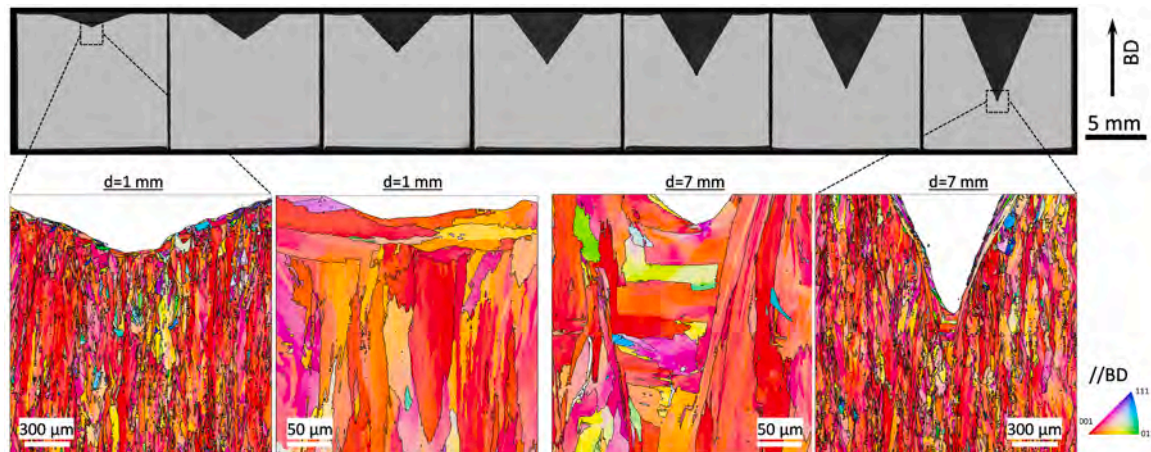


Fig. 2. Stitched optical micrograph of the V-notch samples before heat treatment with representative IPF maps superposed by grain boundary plots for V-notch samples with notch depth  $d = 1$  and 7 mm.

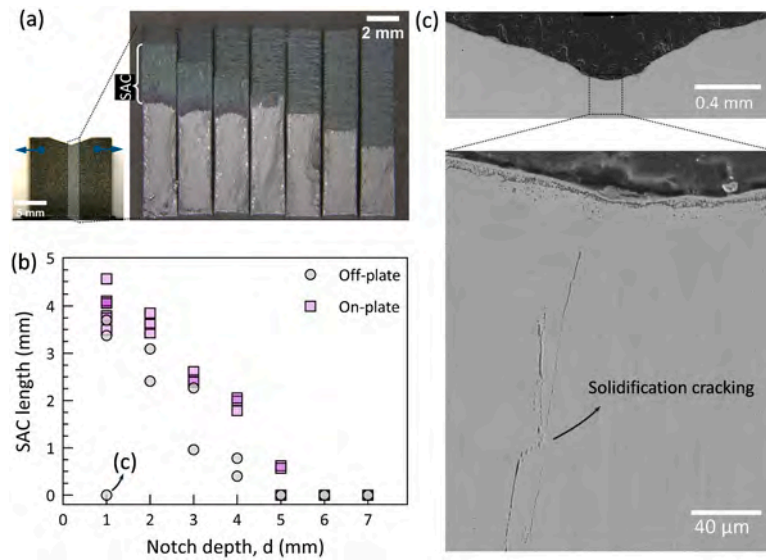


Fig. 3. SAC of V-notch samples from heat treatment at 1120 °C/2 h, (a) stereo optical micrograph of the mechanically opened fractures of off-plate samples, (b) plot of SAC length as a function of notch depth for both off- and on-plate samples (each data point corresponds to a distinct V-notch sample), (c) stretched secondary electron SEM micrograph of a d = 1 mm V-notch sample absent from SAC.

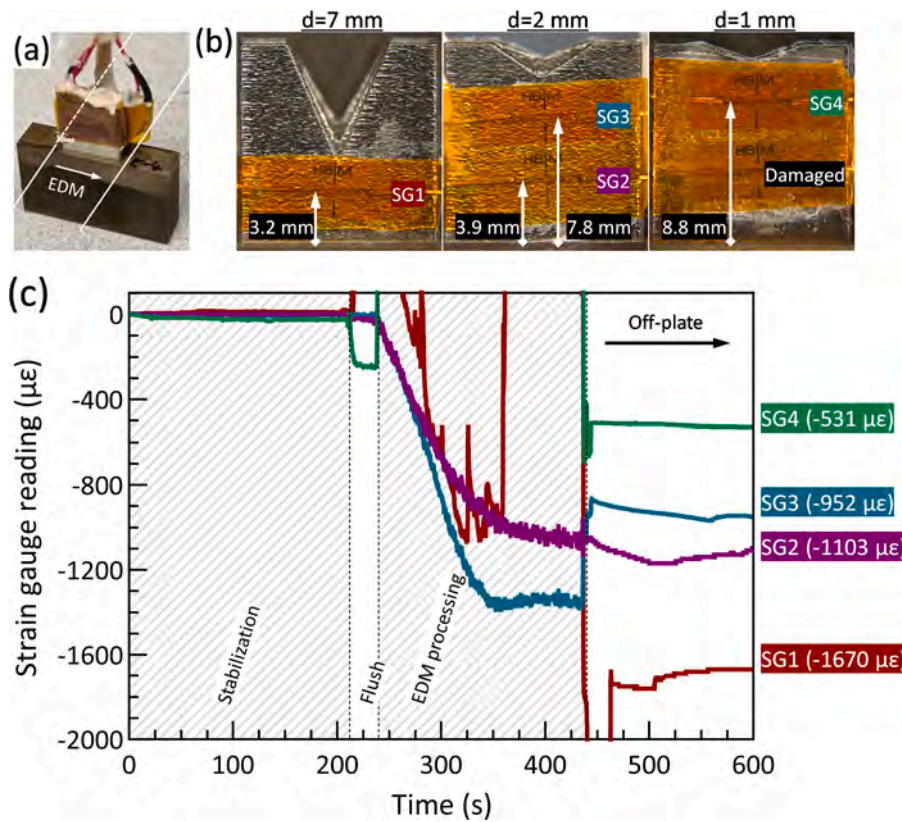
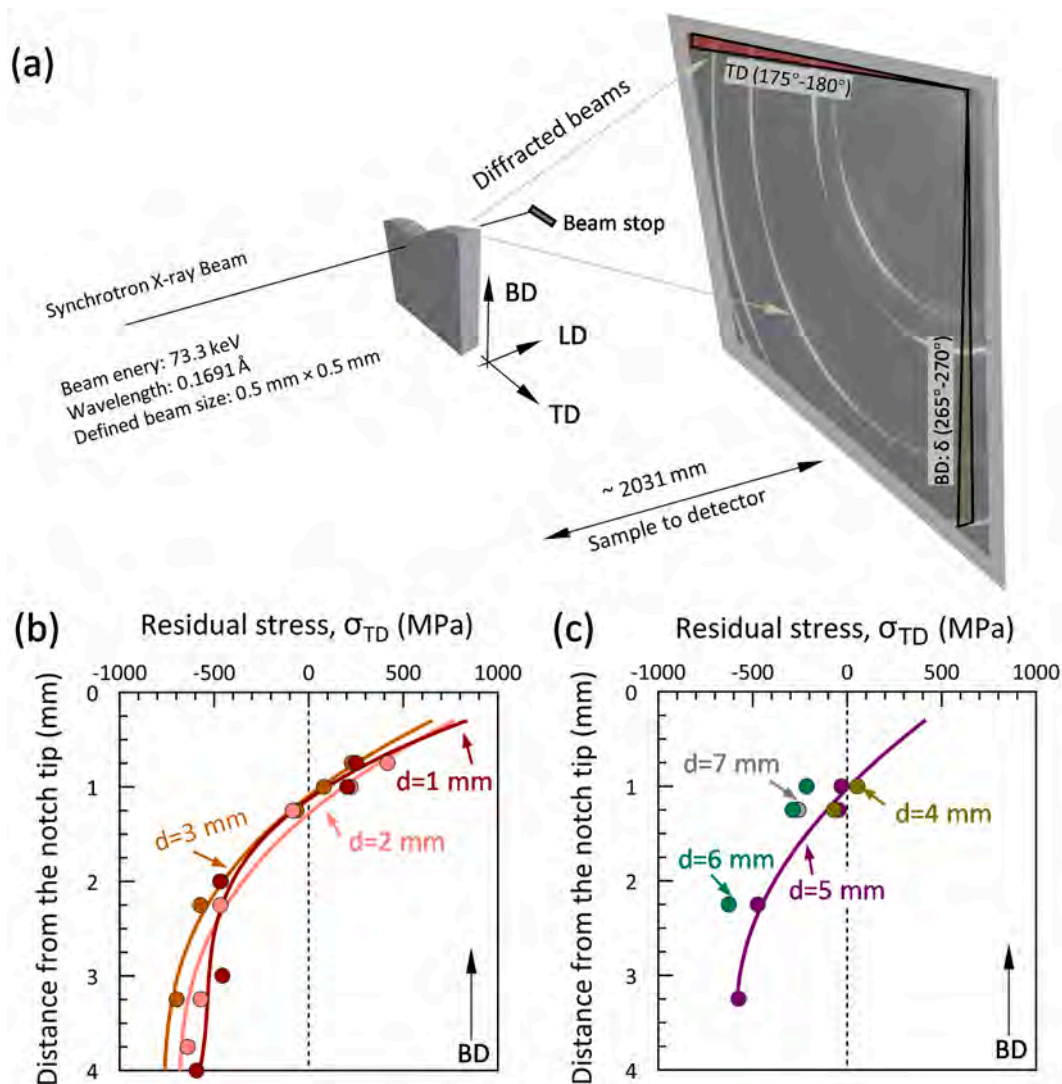


Fig. 4. Transverse strain measurement of cutting V-notch sample off build plate, (a) photo of strain gauge attached sample to be cut by EDM, (b) stereo optical micrograph of the positioning of strain gauges on various V-notch samples, and (c) strain gauge reading as a function of time during EDM process.

using a Pseudo-Voigt function implemented in the lmfit Python library [41]. The lattice strain  $\epsilon^{311}$  was then calculated using  $\epsilon^{311} = (\epsilon^{311} - \epsilon_0^{311})/\epsilon_0^{311}$ , where  $\epsilon_0^{311} = 1.085101 \text{ \AA}$  was obtained from an average derived through a  $d$ -versus- $\sin^2\psi$  analysis using  $5^\circ$  wide bins at different  $\psi$ -angles [42]. The residual stress along TD was obtained by applying Hooke's law in plane stress assuming the  $\sigma_{LD} = 0$ , expressed as  $\sigma_{TD} = \frac{E^{311}}{(1-\nu^2)} (\epsilon_{TD}^{311} + \nu\epsilon_{BD}^{311})$ , where  $\nu$  is taken as 0.3 and  $E^{311} = 175.8 \text{ GPa}$ ,

calculated using Kröner's model with single crystal compliances at room temperature from Bayerlein et al. [43].

Fig. 5(b) and (c) show the transverse residual stress as a function of distance from the notch tip for shallow and deep notches, respectively. Because the X-ray beam only partially entered the sample near the notch tip, measurements in these surface regions were unreliable; therefore, the first valid residual stress data were obtained approximately 0.75–1.0



**Fig. 5.** Residual stress measurement in the TD component using high-energy synchrotron X-ray diffraction. (a) Schematic of the experimental setup showing the beam configuration and sample orientation with the BD aligned vertically. (b–c) Transverse residual stress as a function of distance from the notch tip for samples with (b) shallower notches ( $d = 1/2/3$  mm) and (c) deeper notches ( $d = 4/5/6/7$  mm). The uncertainty in residual stress from peak-center fitting is approximately 0.7 MPa. The solid lines in (b) and (c) are from second-order polynomial fitting, provided as a guide for the eye.

mm from the tip. Overall, high tensile transverse residual stresses develop near the notch tip and decrease with distance, eventually becoming compressive. The solid lines in Fig. 5(b-c) represent second-order polynomial fits, included only as a guide to the eye. In general, as notch depth increases, the tensile transverse residual stress near the notch tip, i.e. the driving force for SAC initiation, decreases significantly.

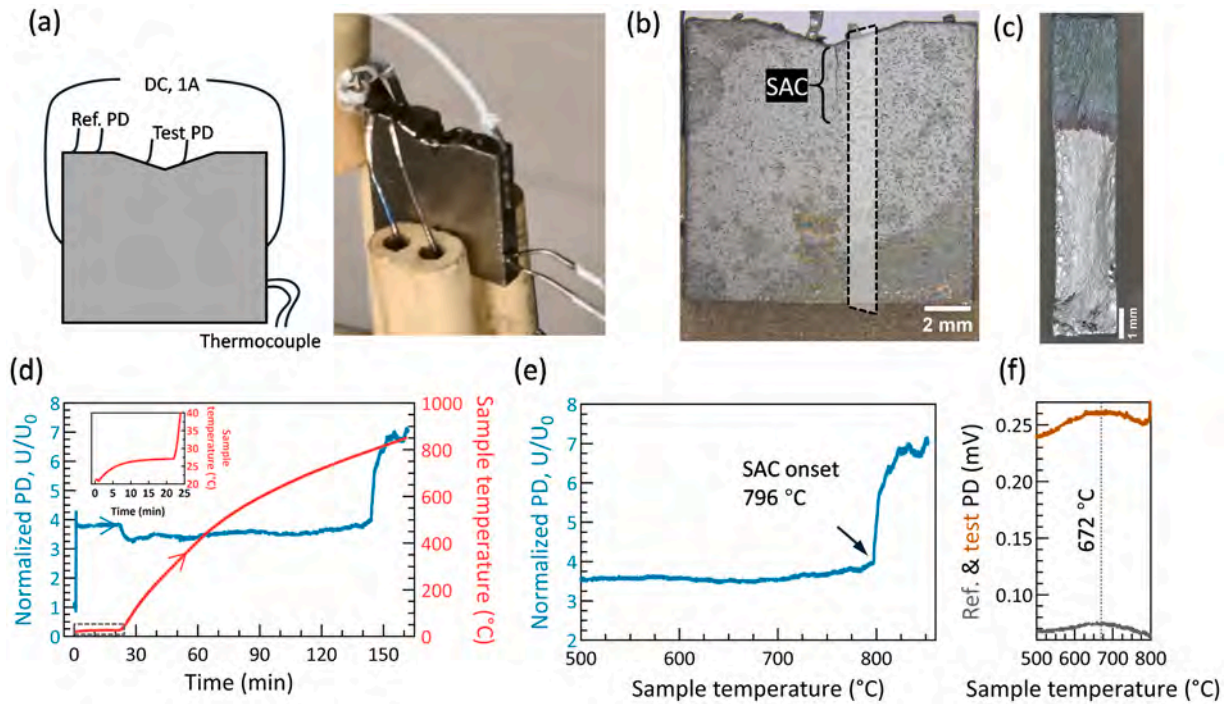
### 3.3. Onset of SAC

Fig. 6 shows the use of the DCPD technique to monitor the initiation of SAC in a V-notch sample with  $d = 1$  mm. As shown in Fig. 6(a), a constant DC current (1 A) was applied through the sample. The normalized potential drop (PD) was calculated as a ratio between two simultaneously measured PDs:  $U_0$ , at the reference position where SAC is unlikely to occur, and  $U$ , the test position near the notch tip where SAC is expected to initiate. After instrumentation, the sample was placed in a chamber furnace. The heat treatment cycle consisted of multiple stages: an initial  $\sim 20$  min stabilization period with the furnace off, followed by continuous heating to 1120 °C over approximately 270 min.

The inset in Fig. 6(d) shows the sample temperature response during the first 25 min. During the first  $\sim 22$  min, Joule heating from the

applied 1 A DC current raises the temperature only slightly, from approximately 21 °C to 27 °C, after which the temperature stabilizes. After  $\sim 22$  mins, the subsequent rapid temperature increase is predominantly governed by furnace heating, with the Joule heating contribution remaining negligible. The sample temperature was monitored using thermocouples spot-welded directly onto the specimen surface. Then this sample was then held at 1120 °C for 120 min, followed by furnace cooling. After approximately 162 min from the start of the heating, the PD signal became heavily distorted due to the extensive SAC occurrence, and thus the curves in Fig. 6(d) and (e) were clipped at that point.

Fig. 6(b) and (c) show the resulting SAC after the full heat treatment cycle, on the front surface and SAC fracture opened by mechanical tearing, respectively. By taking the ratio  $U/U_0$ , the influence of temperature, composition, and phase evolution is largely compensated, so that subsequent changes in the ratio predominantly reflect geometric changes associated with crack initiation and growth. Consequently, as shown in Fig. 6(e), the normalized PD remained stable until the temperature reached  $\sim 796$  °C, where a sharp increase occurred, indicating the onset of SAC. In the raw reference and test PD-temperature plot (Fig. 6(f)), a characteristic increase and subsequent decrease in signal is observed within the 500 to 800 °C range. For example, the test PD



**Fig. 6.** Setup and results from DCPD measurement for SAC occurrence, (a) schematic drawing of the connecting wires together with a photo of instrumented DCPD sample of  $d = 1$  mm before heat treatment, (b) the front view of this sample after the full heat treatment cycle showing SAC, and (c) stereo micrograph showing SAC fracture opened by mechanical tearing (d) double-Y axis plots of normalized PD and sample temperature as a function of time, the inset shows the enlarged view of sample temperature response in the first 25 min (e) plot of normalized PD as a function of sample temperature highlighting the SAC onset, and (f) plots of reference and test PD as a function of temperature in 500–800 °C temperature range.

increases from 0.239 mV at 500 °C to a peak of 0.261 mV at 672 °C, i.e. an approximate 9.2% increase, before declining. This trend reflects changes in electrical resistivity associated with  $\gamma'$  phase transformation. In nickel-based superalloys that initially contain  $\gamma'$ , heating leads to  $\gamma'$  dissolution, resulting in a drop in resistivity. For as-built PBF-LB microstructures that initially lack  $\gamma'$ , however, the rise in resistivity starting near 500 °C features  $\gamma'$  nucleation [44].

In this study the increment of PD under DC conditions corresponds to the electrical resistivity and agreed with its value measured in literature.

For instance, on the electrical resistivity measurement with temperature from Markanday et al. [25], the peak resistivity (approximately 1710 n $\Omega$ ·m) has increased 9.6% compared to 500 °C (approximately 1560 1710 n $\Omega$ ·m) of an IN738LC superalloy heated at 5 K/s from as-built condition, though the peak appeared at a higher temperature.

While the DCPD method can effectively determine the SAC onset temperature, it does not provide insight into the subsequent propagation of SAC. To overcome this limitation, *in situ* monitoring of V-notch samples during induction heating was performed. The experimental

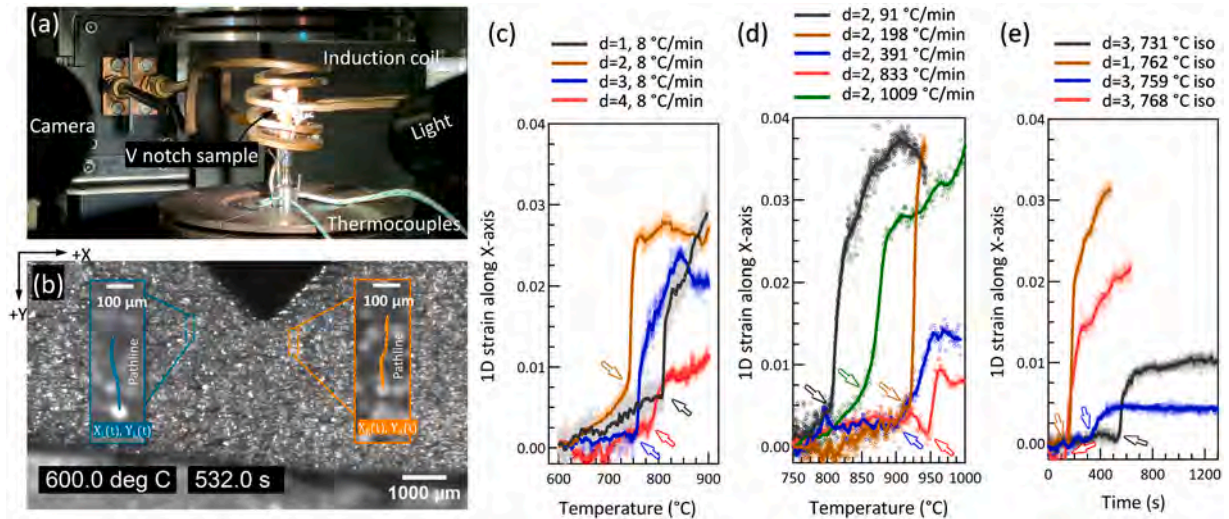


**Fig. 7.** (a) Photo of the experimental setup for *in situ* induction heating of V-notch samples. (b) A frame from the high-resolution image sequence recorded during heating, showing a highlighted particle pair with tracked trajectories superimposed. Plot of 1D axial strain along X-axis as a function of temperature, white arrows indicate SAC onset temperature, for (c) different notch depths at an identical heating rate of 8 °C/min, (d) identical notch depths with different fast heating rates, and (e) plot of one-dimensional axial strain along the X-axis as a function of time for the isothermal conditions.

setup, as in Fig. 7(a), shows a V-notched specimen clamped within an induction heating coil using an austenitic steel holder. A high-resolution camera records the surface evolution during heating. High-magnification image sequences were analyzed using the TrackMate plugin [45,46] in Fiji, applying a Kalman filter tracker to follow the motion of distinct surface features on either side of the notch, as illustrated in Fig. 7(b). Tracked trajectories ( $X_L(t)$ ,  $X_L(t)$ ) and ( $X_R(t)$ ,  $X_R(t)$ ) were used to compute the 1D axial strain along the X-axis between particle pairs, expressed as:  $\epsilon_{xx}(t) = \frac{[X_R(t) - X_L(t)] - [X_R(t_0) - X_L(t_0)]}{X_R(t_0) - X_L(t_0)}$ .

It should be noted that this analysis is qualitative rather than quantitative, due to noise introduced by evolving surface conditions such as glowing and oxidation. Fig. 7(c) shows the resulting 1D strain vs. temperature for samples with various notch widths heated from 600 °C to 900 °C at a constant rate of 8 °C/min. Each curve represents the temperature-dependent strain response. Initially, strain increases gradually primarily due to thermal expansion. Upon reaching the SAC onset temperature, a sharp increase in 1D strain is observed (indicated by arrows), corresponding to widening at the notch tip due to SAC initiation. Under faster heating conditions (Fig. 7(d)), the 1D strain vs. temperature trends resemble those observed at slow heating rates. A general observation is that SAC onset occurs at higher temperatures in these cases. In Fig. 7(e), 1D strain is plotted against time for isothermal heating conditions. Minimal strain increase is observed prior to SAC onset due to limited thermal expansion. A second rise in strain following the sharp increase indicates SAC widening. In general, SAC formation introduces several percent of 1D strain, which is difficult to accommodate at elevated temperatures. For comparison, tensile elongation at fracture along the transverse direction in PBF-LB IN738LC is limited to ~5.2% at 800 °C and ~2.8% at 900 °C [38].

Fig. 8 presents the evolution of SAC length as a function of relative time during *in situ* induction heating, with the time of SAC onset reset to zero. Three different heating scenarios are shown: a slow heating rate of 8 °C/min for various notch depths, fast heating rates for identical notch depth, and isothermal conditions. For the fast-heating rate, it was calculated via linear regression of the temperature over time, from 50 °C below the SAC onset temperature up to the onset temperature, determined as 91, 198, 833, and 1009 °C/min. For each case, a time-lapse series of key frames (frames 1–5) captures the progression of SAC from initiation to propagation, where the circle indicates the SAC tip. To enhance visibility, an optical flow plot (from frame 5 to frame 1), with color representing direction and brightness indicating displacement magnitude, was generated using Gunnar Farneback's method [47] built into the OpenCV Python library. Animated image frames capturing the SAC events are included in the supplementary materials. Generally, once SAC initiates, it propagates rapidly. SAC growth rates were estimated by linear regression over the first 1 mm of crack growth. It should be noted that the advancing SAC tip was identified from high-resolution image frames on one surface representing the overall propagation rate. The propagation rates of possible multiple SACs or branches cannot be distinguished individually.

Under the identical slow heating rate of 8 °C/min (Fig. 8 (cont.1)), V-notch samples with varying notch depths ( $d = 1, 2, 3, 4$  mm) were examined. At this heating rate, shallower notches (e.g.,  $d = 1$  mm) show significantly faster SAC growth (e.g., 262  $\mu\text{m/s}$ ), while deeper notches exhibit slower rates ranging from 66 to 113  $\mu\text{m/s}$ . In contrast, under various rapid heating conditions for  $d = 2$  mm samples, SAC propagation becomes remarkably faster as the heating rate increases. At heating rates of 91, 198, 833, and 1009 °C/min, the SAC growth rates for the first 1 mm of crack length reach 553, 1323, 1007, 3790, and 3670  $\mu\text{m/s}$ , respectively. Notably, although the heating rate increases by a factor of 126 (from 8 to 1009 °C/min), the SAC growth rate increases by >35-fold (from 103 to 3670  $\mu\text{m/s}$ ). Although fast heating reduces the time available for residual-stress relaxation and  $\gamma'$  precipitation, the markedly higher crack growth rates still indicate that reaching elevated temperatures is the primary driver of SAC propagation.

Additionally, to further decouple thermal effects from the influence of heating kinetics, a series of isothermal experiments were conducted at various temperatures, as shown in Fig. 8 (cont.2). Even under constant temperatures (e.g., 731, 762, 759, 768 °C), SAC can still be activated and propagate, though at relatively slower growth rates. For example, under isothermal conditions at 762 °C with a  $d = 1$  mm sample, the growth rate is approximately 167  $\mu\text{m/s}$ . For samples with the same notch depth ( $d = 3$  mm), lower isothermal temperatures generally lead to slower SAC growth rates. At 731 °C, the growth rate is only 38  $\mu\text{m/s}$ , while at 759 °C and 768 °C, it increases to 106  $\mu\text{m/s}$  and 83  $\mu\text{m/s}$ , respectively.

Although the comparison is qualitative, these data highlight that SAC propagation is highly temperature sensitive. SAC growth rates increase abruptly once a critical temperature threshold is surpassed. This indicates that elevated temperature, rather than prolonged exposure time, is the primary driver of rapid SAC propagation.

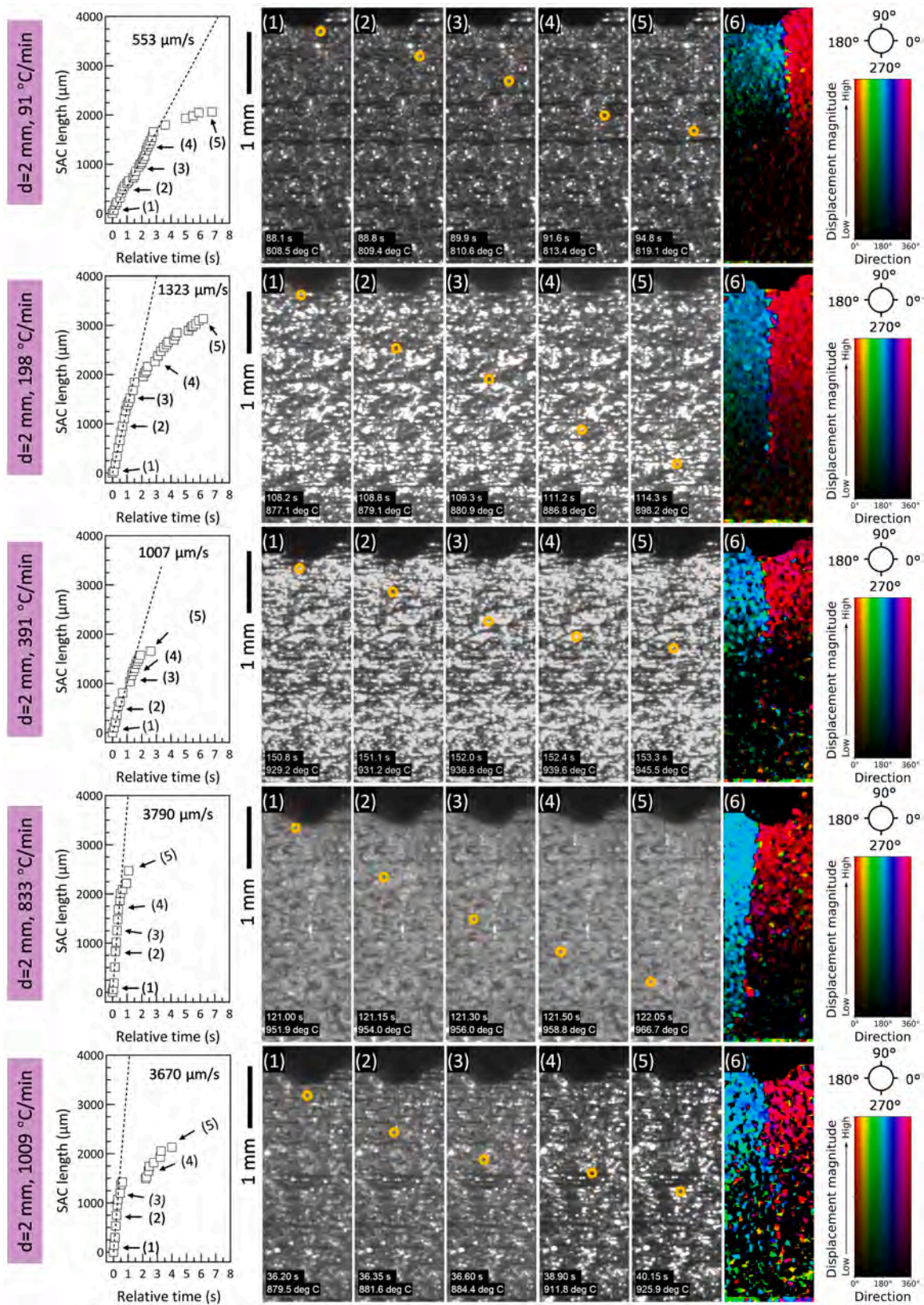
### 3.4. SAC susceptibility map of PBF-LB IN738LC

Fig. 9 presents the SAC susceptibility map of the PBF-LB IN738LC superalloy, with heating curves plotted from a baseline temperature of 713 °C to the SAC onset, marked by cross symbols. Overlaid on the map is the experimentally determined time-temperature-transformation (TTT) diagram for  $\gamma'$  precipitation, adapted from [48]. The baseline of 713 °C corresponds to the temperature below which no  $\gamma'$  formation is expected, even after 10,000 min of isothermal exposure, according to the referenced TTT data. The map includes markers indicating whether  $\gamma'$  was identified (solid circles) or not (open circles). It is worth noting that  $\gamma'$  identification in the reference TTT diagram was based on SEM micrographs and or superlattice reflections in selected area electron diffraction in transmission electron microscopy for finer  $\gamma'$ . This plot outlines the “C-curves” widely used in post-weld heat treatment investigations in defining the minimum heating rate without occurrence of SAC [49].

In the fast induction heating scenarios, a clear trend emerges: higher heating rates result in higher SAC onset temperatures. The highest observed SAC onset temperature occurred at 951 °C under an extremely fast heating rate of 833 °C/min. It is interesting to note that for the 1009 °C/min condition, although the critical heating rate is greater than 833 °C/min, the SAC onset temperature was found at 879 °C apparently lower than 951 °C, as a consequence of accidentally delayed heating for the first 0.4 min where the temperature stayed at approximately 720 °C. Under these continuous heating conditions, SAC initiation should be interpreted as a kinetically controlled process rather than a temperature-triggered event. Consequently, the experimentally determined SAC onset temperature represents an apparent, heating-rate-dependent value rather than a threshold temperature. At lower heating rates, sufficient time is available for  $\gamma'$  formation and damage accumulation within the intermediate temperature range, enabling SAC initiation at relatively lower temperatures. In contrast, rapid heating compresses the incubation stage, requiring higher temperatures to accelerate the kinetics of  $\gamma'$  formation and strain localization, leading to a higher measured onset temperature.

Stress relief treatments, typically performed at lower isothermal temperatures, have been proposed as a solution to mitigate SAC. Risse [35] reported, based on curvature angle measurements of as-built samples annealed on the build plate, that stress relief begins around 500 °C and reaches a plateau above 900 °C. While these treatments can relieve residual stress, preventing SAC during such cycles is not straightforward. In this study, isothermal treatments at 768, 762, 759, and 731 °C all led to SAC, although the incubation time increased with decreasing isothermal temperature. These conditions fall within the  $\gamma'$  precipitation regime eventually.

For samples heated at 8 °C/min, a rate comparable to industrial practice, no consistent trend was observed between SAC onset temperature and notch depth. The lack of correlation with notch geometry, despite its strong influence on residual stress, indicates that SAC onset is



**Fig. 8.** SAC propagation behavior under fast heating conditions for notches with  $d = 2$  mm. For each heating rate, the SAC length is plotted as a function of relative time, where the SAC onset time is defined as  $t = 0$ . The slope of the dashed line represents the estimated average crack propagation rate during the first 1 mm of SAC growth. Image frames (1) - (5) present representative *in situ* optical images capturing successive SAC growth events with yellow circles marking the advancing crack tip. Panel (6) shows the corresponding displacement magnitude (indicated by brightness) and direction (indicated by color) maps, illustrating strain localization caused by crack opening.

**Fig. 8 (cont.1).** SAC propagation behavior under slow heating conditions for various notch depths. For each notch depth, the SAC length is plotted as a function of relative time, where the SAC onset time is defined as  $t = 0$ . The slope of the dashed line represents the estimated average crack propagation rate during the first 1 mm

of SAC growth. Image frames (1) - (5) present representative *in situ* optical images capturing successive SAC growth events with yellow circles marking the advancing crack tip. Panel (6) shows the corresponding displacement magnitude (indicated by brightness) and direction (indicated by color) maps, illustrating strain localization caused by crack opening.

**Fig. 8 (cont.2).** SAC propagation behavior under isothermal conditions. For each isothermal condition, the SAC length is plotted as a function of relative time, where the SAC onset time is defined as  $t = 0$ . The slope of the dashed line represents the estimated average crack propagation rate during the first 1 mm of SAC growth. Image frames (1) - (5) present representative *in situ* optical images capturing successive SAC growth events with yellow circles marking the advancing crack tip. Panel (6) shows the corresponding displacement magnitude (indicated by brightness) and direction (indicated by color) maps, illustrating strain localization caused by crack opening.

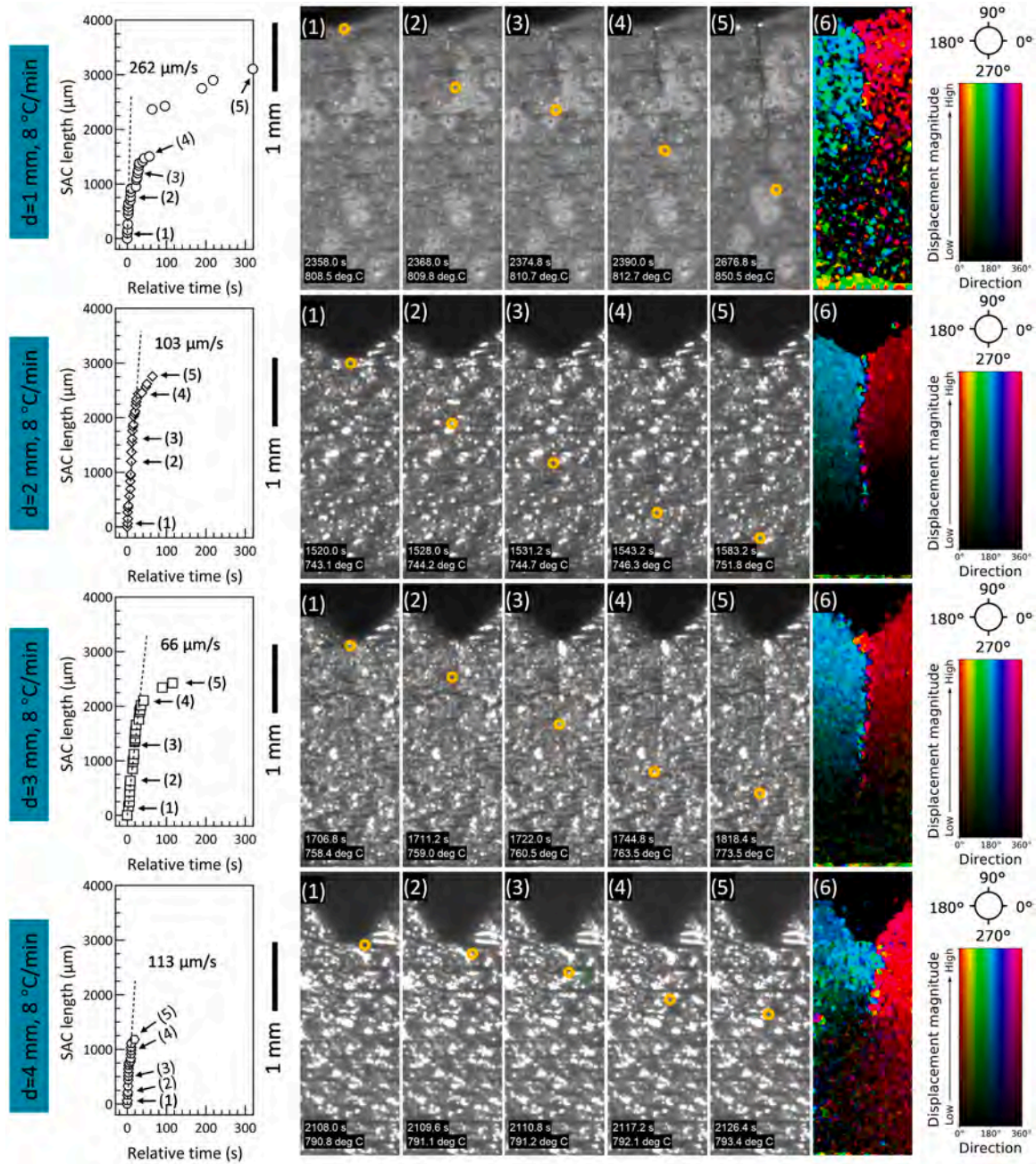


**Fig. 8.** (continued).

likely not controlled by the residual stress state. The onset temperatures cluster within the  $\gamma'$  precipitation regime and shift systematically with heating rate, supporting the conclusion that SAC initiation is governed primarily by  $\gamma'$  precipitation kinetics. Instead, residual stress strongly influences the subsequent SAC growth rate, as higher stresses promote faster crack propagation (see Fig. 8 (cont.1)). Consequently, for the V-notch samples examined in this study, it is not practically feasible to avoid SAC by bypassing the critical  $\gamma'$  precipitation regime.

### 3.5. Characterization of SAC

Fig. 10 shows cross-sectional views of SAC morphologies in V-notch samples after heat treatment at  $1120$  °C for 2 h, using stitched secondary electron SEM micrographs of chemically etched surfaces near the notch tips. Fig. 10(a-g) illustrates a progression from shallow to deep notches ( $d = 1-7$  mm), while Fig. 10(a1-a3, e1, f1, g1) highlights microstructural details for representative samples. In the shallow notches ( $d = 1-4$  mm),

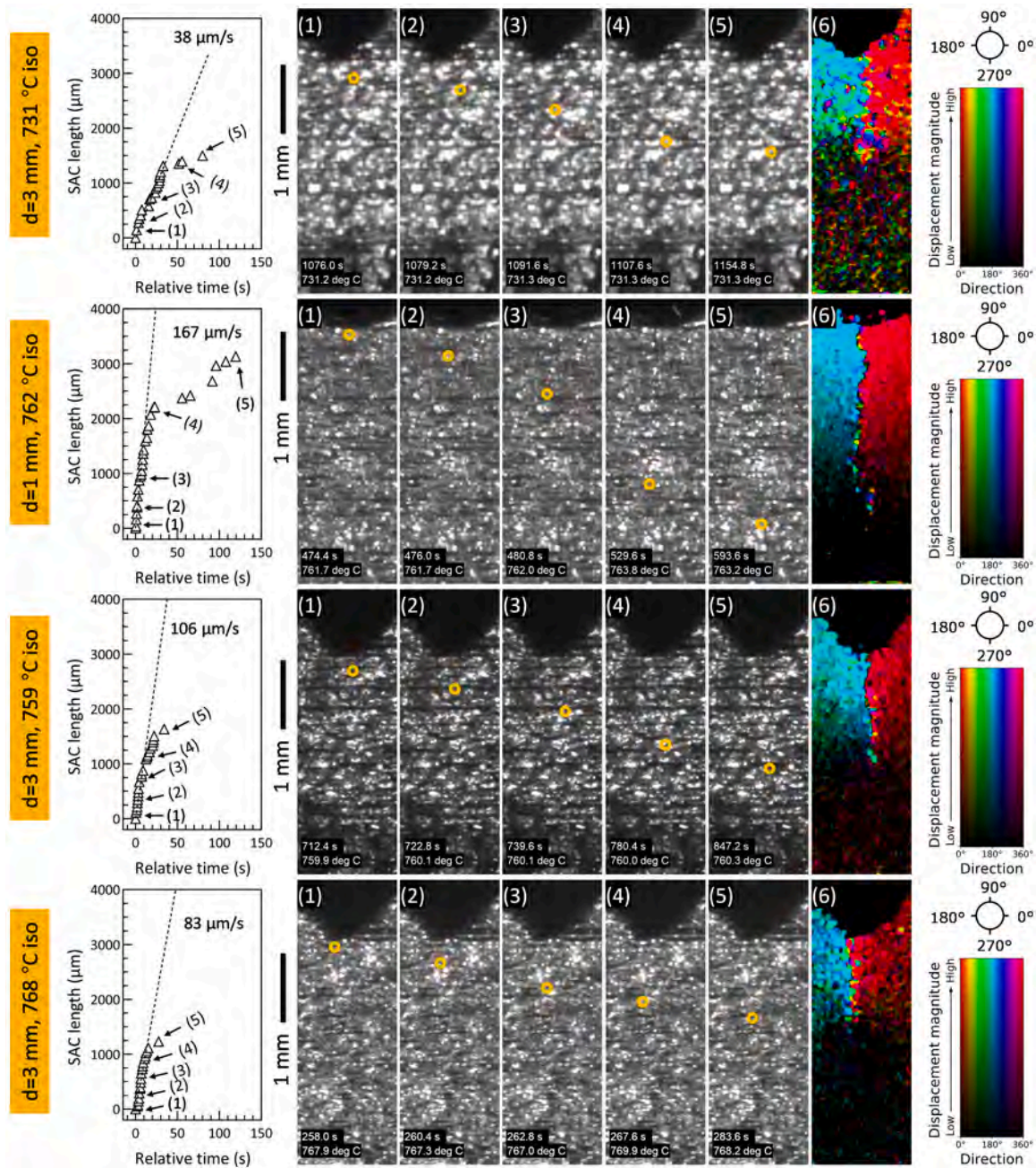


Fig. 8. (continued).

extensive SAC cracks are observed. The SAC exhibits opening widths of several tens of micrometers, with heavily oxidized surfaces. The oxide layer was measured to be a few to approximately  $20$   $\mu\text{m}$ . Controlled by solid-state diffusion,  $\gamma'$ -depleted zones are present along with oxide scale growth, forming a few-micrometer-wide zone with apparently finer  $\gamma'$  near the crack tip (detailed in Fig. 10(a3)).

In contrast, samples with deeper notches ( $d \geq 5$  mm) show no SAC formation. Enlarged views Fig. 10(e1, f1, g1) reveal pre-existing defects such as pores and solidification cracks. However, there is no clear evidence that the presence of these defects alone suppresses SAC, as the coexistence of solidification cracks and SAC is also observed in Fig. 10(a1). A plausible explanation is that the size, density and location of solidification cracks influence SAC occurrence. Since the observations are based on 2D sections, the true three-dimensional size and connectivity of solidification cracks cannot be accurately assessed. Therefore, their exact influence on SAC remains uncertain and requires further

investigation. In addition, the limitation of this observation makes it difficult to determine whether the apparent presence of multiple cracks (e.g., Fig. 10(a-d)) corresponds to independent SAC initiation events or branching of a single SAC.

Fig. 11 presents the morphology of SAC in a  $d = 1$  mm V-notch sample after heat treatment at  $1120$  °C for 2 h. The sample was mechanically forced open after SAC to expose internal crack features. Fig. 11(a) shows a stereo optical image, and Fig. 11(b) provides a stitched secondary electron SEM image capturing the SAC and the surrounding transition region. Enlarged SEM views in Fig. 11(c-e) highlight different zones of microstructures. Fig. 11(c) and (d), corresponding to SAC propagation regions at approximately 77% and 94% of the total crack length, respectively, revealing surface oxidation and the presence of oxide films along the crack path.

However, distinct morphologies are observed between these two regions. At 77% of the SAC length (Fig. 11(c)), the surface appears

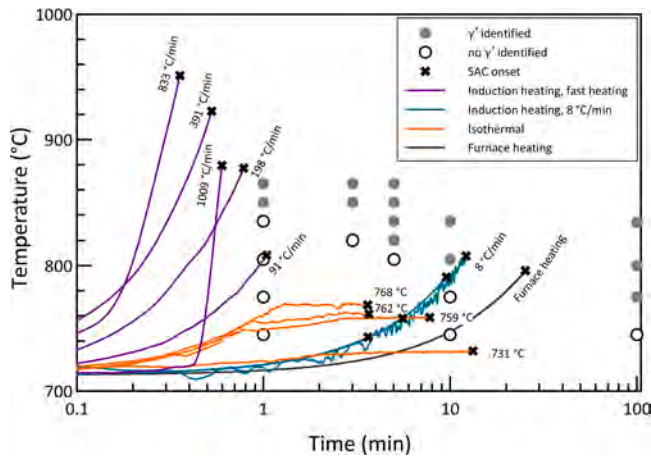


Fig. 9. SAC susceptibility map of V-notch PBF-LB IN738LC superalloy from a baseline temperature of 713 °C, where the experimentally determined TTT diagram is from reference [48].

relatively flat, resembling a compacted oxide layer. In contrast, at 94% (Fig. 11(d)), a clear intergranular cracking with oxidation decorated feature can be identified. Similar intergranular fractography was observed in IN738LC PBF-LB superalloys tested at elevated temperatures, with the loading direction perpendicular to the BD [50]. In Fig. 11(e), taken from a fracture caused by mechanical tearing at room temperature, typical transgranular fracture features are displayed. The compacted surface seen in Fig. 11(c) suggests that oxide scale growth played a critical role in SAC propagation. The growth of oxides has likely had a wedging effect, promoting further crack opening and propagation.

The oxide composition was examined using EDS analysis. Fig. 12 presents a cross-sectional characterization of SAC morphology and associated oxidation following heat treatment at 1120 °C for 2 h. Fig. 12(a) shows a stitched secondary electron SEM micrograph illustrating the full SAC path extending from the notch tip. Fig. 12(b-d) highlight three distinct regions along the SAC: at distances of 0.27 mm, 2.98 mm, and 3.54 mm from the notch tip, corresponding to approximately 8%, 82%, and 97% of the total SAC length, respectively, together with EDS elemental maps for O, Ti, Cr, and Al.

Near the notch tip (Fig. 12(b)), oxidation is intense, and oxide scale is continuous, with an oxide thickness of approximately 12 μm on one side. Further along the crack (Fig. 12(c)), the oxides grew and filled the gap in between the SAC with a total thickness of approximately 16 μm across both sides. Closer to the SAC tip (Fig. 12(d)), the oxide scale appears more discontinuous and significantly thinner, measuring approximately 8 μm across both sides based on the secondary electron micrograph. From the EDS maps, regions Fig. 12(b) and Fig. 12(c) show similar oxide configurations: a Ti-rich outermost layer, a Cr-rich intermediate layer, and Al-rich oxides closest to the bulk. However, region Fig. 12(d) lacks a Cr-rich oxide layer, suggesting that oxidation in this location occurred at a different temperature range, likely one in which Cr-rich oxides were energetically less favorable to form.

The surface chemistry of the mechanically opened SAC fracture was examined by XPS at three areas, referred to as “dark”, “brown”, and “light”, representing the SAC initiation, the transition zone, and the mechanically fractured metal surface, respectively. The normalized O 1s survey spectra are shown in Fig. 13. Two O 1s components at binding energies of 529.9 eV and 531.1 eV were identified, corresponding to Cr oxides [51] and Al oxides [52], respectively. A pronounced Al-oxide peak was observed from the “brown” area, consistent with the cross-sectional EDS mapping near the notch tip shown in Fig. 12(d), although potential artefacts from surface oxidation during XPS analysis should be considered. Depth profiling of the O 1s signal to a depth of 300 nm for the “dark” and “light” areas (Fig. A2 in the Appendix) shows that the Cr-oxide component increases rapidly with etching depth in the

“dark” area and decreases quickly in the “light” area.

Fig. 14 shows the cross-sectional morphology of SAC in a  $d = 2$  mm V-notch sample subjected to rapid induction heating at 200 °C/min to 900 °C. Owing to the fast heating and cooling, oxide scale formation is largely suppressed, allowing clearer visualization of the underlying fracture. Fig. 14(a) presents a stitched secondary electron SEM micrograph of the as-polished surface, clearly revealing the SAC path. The inset highlights a fracture region with interdendritic features, resembling the widely reported morphology of solidification cracking as in reference [53–55].

Fig. 14(b) and (c) show enlarged views of the mid-section and tip of the SAC, respectively, together with IPF coloring maps derived from EBSD scans, using BD as the reference axis for coloring. The IPF maps confirm a dominant intergranular fracture mode, with cracks consistently propagating along grain boundaries. In PBF-LB superalloys, such boundaries correspond to “solidification grain boundaries” [56], which are located at interdendritic regions. Consequently, it is unsurprising that the SAC fracture surface shows interdendritic features similar to those of solidification cracking. The relatively clean fracture surfaces further suggest that oxide growth occurred after SAC formation, indicating that presence of an oxide layer is not a critical factor in SAC initiation.

Fig. 15(a) presents IPF coloring and Kernel Average Misorientation (KAM, 1st order neighbors) maps near the SAC initiation sites under different thermal histories. Similar to the intergranular cracking observed further along the SAC, intergranular cracking remains predominant near the initiation sites. However, transgranular cracking also occurs, as seen in the inset showing crystal shapes viewed from the surface normal in the 762 °C isothermal and 91 °C/min heating conditions, with neighboring misorientations of 8.2° and 5.2°, respectively, calculated from their Euler angles. These transgranular cracks are accompanied by pronounced localized deformation, as indicated by the black arrows in the corresponding KAM maps. Although transgranular cracking is less energetically favorable at the elevated temperature, it can be developed due to the rapid SAC growth rate.

Compared to the as-built condition, the SACed samples exhibit a general reduction in KAM values. Some regions, indicated by white arrows, show significantly decreased misorientation, suggesting local strain relief. The thermal histories for the SACed samples are presented in Fig. 15(b), focusing on the temperature range above 700 °C. Regardless of the dwell time at elevated temperatures, a notable reduction in KAM is evident, as shown in the histograms in Fig. 15(c). For example, comparing the 8 and 198 °C/min heating conditions, both reaching similar peak temperatures, the slower rate produced a slightly lower geometric mean KAM (0.24°) than the faster rate (0.27°), both being significantly lower than the as-built value (0.41°). The data suggest that most of the KAM reduction occurred prior to SAC initiation, as the 198 °C/min sample experienced SAC onset at 877 °C and reached its peak temperature shortly afterward.

## 4. Discussion

### 4.1. Mechanism of SAC

Compared between the heat treatments on- and off- build plate, the most significant advantage of removing sample off build plate is the relief of residual stress ( $\sigma_R$ ). However, this relief effect was limited to a certain extent. As found in this study, after cutting off the sample, less transverse residual stress was released with increasing distance from the build plate (Fig. 4). These trends were also observed in other studies using neutron diffraction, where high tensile hoop strain (comparable to the transverse direction in this study) was measured near the base of thin-wall PBF-LB structures and was found to decrease sharply with build height [57]. In fact, heat treatment after removal from build plate introduces another well-noticed issue, i.e. distortion [58–60], which is critical to component production. With the layer height increasing, it is

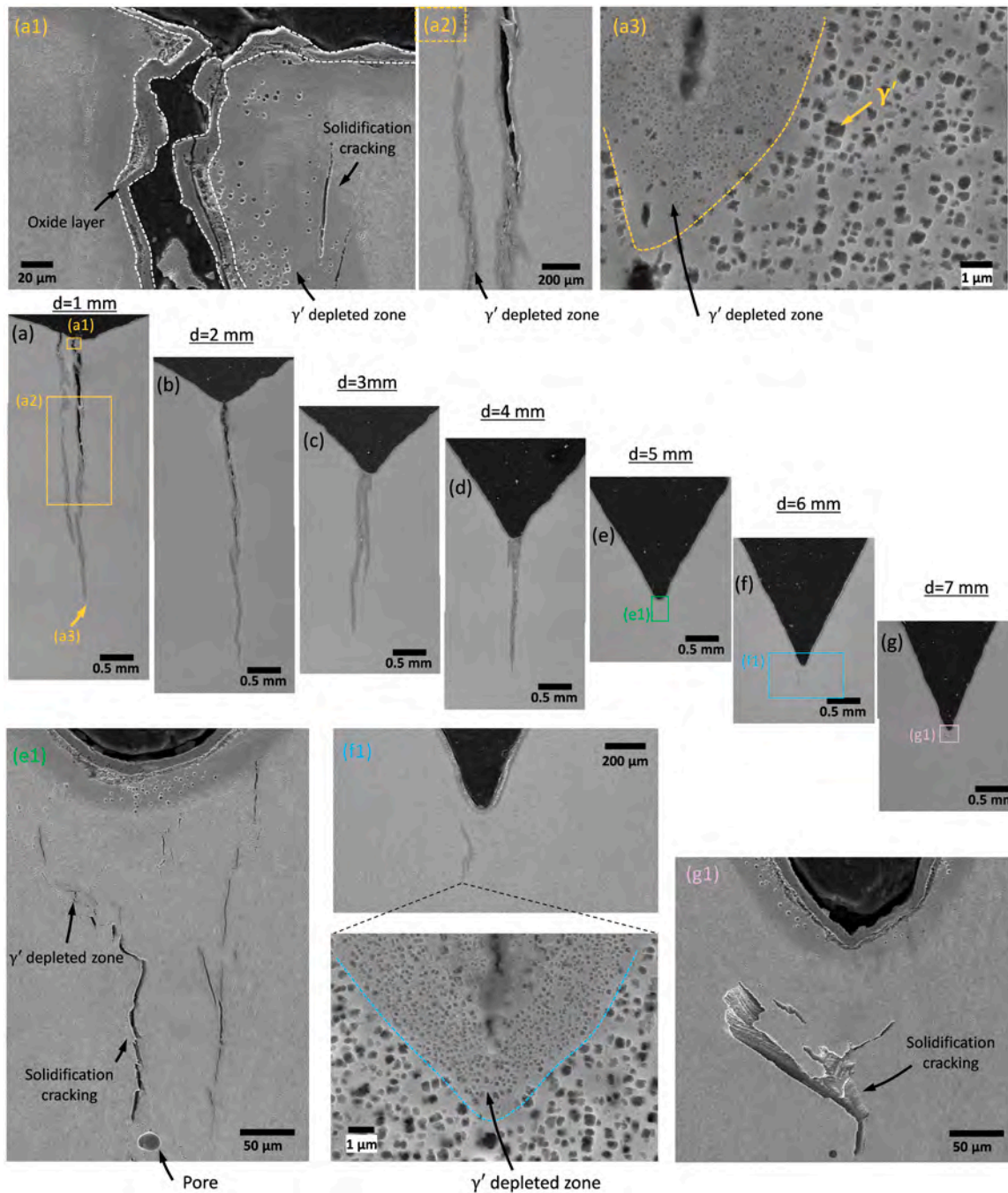


**Fig. 10.** Cross-sectional view of SAC morphology from stitched secondary electron SEM micrographs on the chemically etched surface close to the tips of notches for (a)  $d = 1$  mm, (b)  $d = 2$  mm, (c)  $d = 3$  mm, (d)  $d = 4$  mm, (e)  $d = 5$  mm, (f)  $d = 6$  mm, (g)  $d = 7$  mm V-notch samples, (a1–3) showing enlarged views of  $d = 1$  mm V-notch sample, (e1) showing enlarged view of  $d = 5$  mm V-notch sample, (f1) showing enlarged views of  $d = 6$  mm V-notch sample, and (g1) showing enlarged views of  $d = 7$  mm V-notch sample. All the samples were heat treated at  $1120\text{ }^{\circ}\text{C}/2\text{ h}$ .

well accepted that residual stress build up, thus the highest residual stress appears close to the top surface along BD, as verified by neutron diffraction, contour methods, simulation and neutron Bragg edge imaging [61,62]. All V-notch samples in this study had the same total build height. As a result, deeper notches placed their tips at lower positions within the build, where residual stresses are reduced. Consequently, shallow notches experienced higher tensile residual stresses near the tip, while deeper notches showed much lower stresses, with very deep notches even developing compressive residual stress at the tip, as shown in Fig. 5.

With increasing temperature, SAC onset in the V-notch samples was

determined by *in situ* induction heating and DCPD, occurring between  $\sim 731$  and  $833\text{ }^{\circ}\text{C}$  (Figs. 6–8), which fall within the well-known intermediate-temperature ductility deficit regime of  $\gamma'$ -strengthened nickel-based superalloys. In this temperature range, tensile ductility drops to only a few percent due to grain-boundary sliding and oxidation-assisted grain-boundary weakening [63,64]. Such ductility minima are widely reported in  $\gamma'$ -strengthened alloys, including Monel K-500 [65], alloy 720 Li [66], and PBF-LB IN738LC [50], all of which exhibit severe loss of elongation between  $\sim 600$  and  $900\text{ }^{\circ}\text{C}$  before ductility rises again at higher temperature due to creep-assisted accommodation [66] or recrystallization [67]. Therefore, at the SAC onset temperature, the

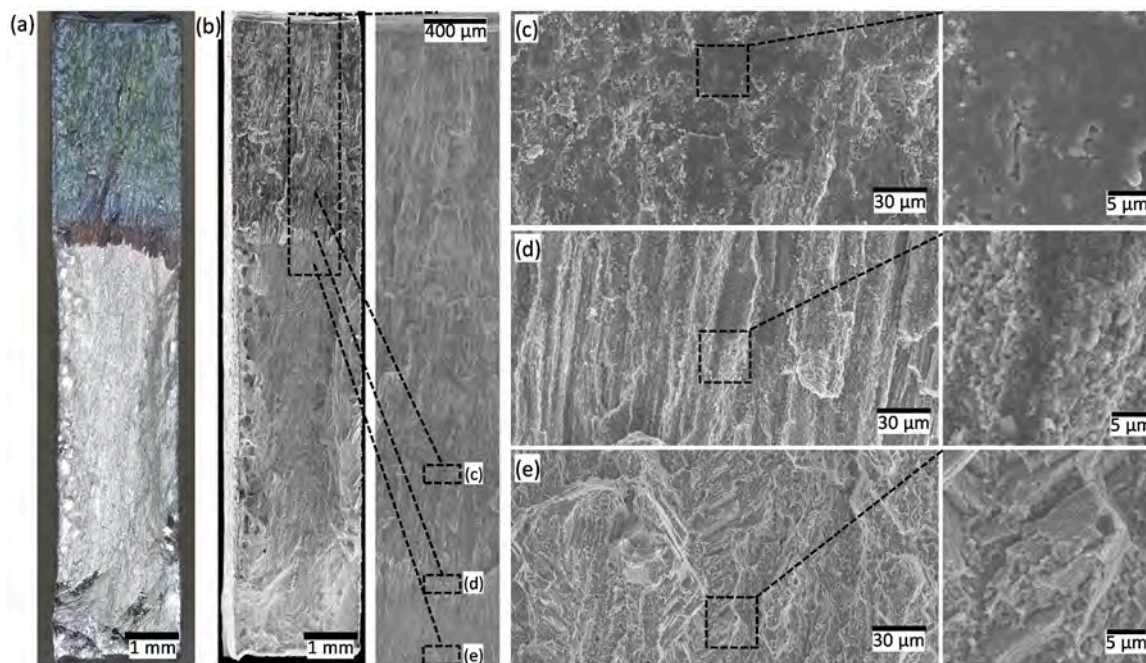


Fig. 11. SAC morphology (mechanically torn open afterward) in a  $d = 1$  mm notch sample heat-treated at  $1120\text{ }^{\circ}\text{C}/2$  h: (a) stereo optical micrograph, (b) stitched secondary electron micrograph highlighting the SAC and transition region, and enlarged views of the (c-d) SAC region and (e) fracture region.

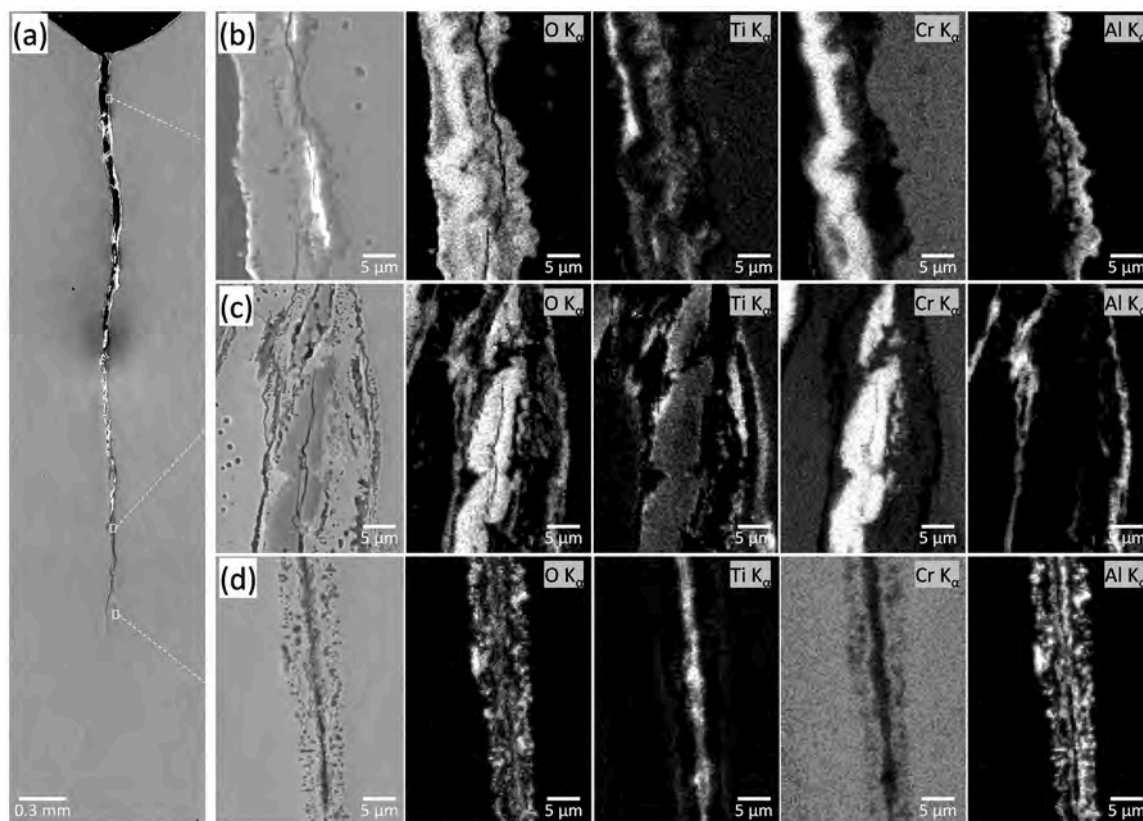


Fig. 12. Cross-sectional view of SAC morphology in a  $d = 2$  mm notch sample heat-treated at  $1120\text{ }^{\circ}\text{C}$  for 2 h. (a) Stitched secondary electron micrograph showing the overall SAC morphology. (b-d) Detailed views of oxidation along the SAC at distances of (b) 0.27 mm (8%), (c) 2.98 mm (82%), and (d) 3.54 mm (97%) from the notch tip, with corresponding EDS elemental maps (O, Ti, Cr, Al). Brighter pixel in the EDS maps indicates higher elemental concentrations.

available ductility is already extremely limited, and even modest local strains cannot be accommodated, promoting intergranular crack (see Figs. 14 and 15) initiation once  $\gamma'$  precipitation further reduces strain

tolerance. The predominantly intergranular crack morphology of SAC observed in this study is similar to that reported for PBF-LB IN738LC under creep deformation [68] and other PBF-LB high-strength

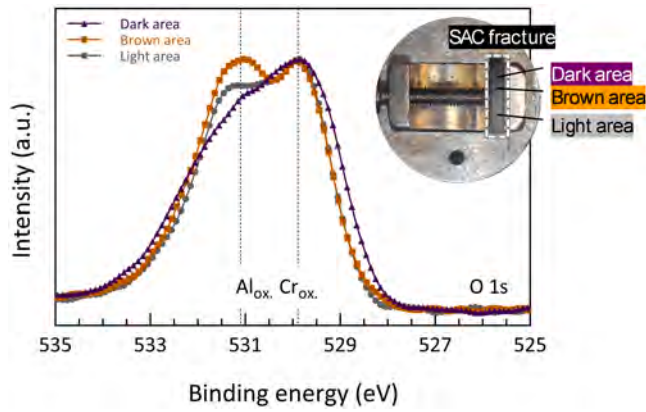


Fig. 13. O 1s XPS survey spectra from the “dark”, “brown” and “light” areas shown in the inset.

superalloys, such as CM247LC [69,70] subjected to creep loading.

The absence of  $\gamma'$  in the as-built microstructure and its emergence during post-processing heat treatment is strongly associated with SAC formation. The TEM observations in Fig. 16 provide direct experimental evidence of nanoscale  $\gamma'$  formation in regions where SAC occurred. The extracted lamellae were taken as immediately as possible after SAC formation to preserve the microstructure close to the crack initiation state. Under the 198 °C/min rapid heating condition, SAC initiated at 877 °C. The subsequent thermal exposure consisted of ~9 s continued heating to 909 °C followed by cooling at ~13 °C/s to 700 °C and

downwards. For the 762 °C isothermal condition, the sample was held approximately 6.57 min beyond the SAC onset time (3.68 min).

Comparison of the HRTEM micrographs (Fig. 16 (b3–c3)) reveals nanoscale  $\gamma'$  in both SACed conditions, identified by Moiré fringes (green arrows) indicating long-range ordering, consistent with  $\gamma'$  identification reported in [11] and [71]. In contrast, only a disordered  $\gamma$  matrix is observed in the as-built condition (Fig. 16(a3)). The corresponding diffraction intensity profiles (Fig. 16 (a5–c5)), extracted along the indicated lines in Fig. 16 (a4–c4), further confirm the presence of  $\gamma'$  in the SACed samples through the appearance of superlattice reflections between adjacent fundamental peaks (black arrows in Fig. 16 (b5 and c5)), which are absent in the as-built condition.

The nanoscale size (2–5 nm) and superlattice intensity indicate early-stage  $\gamma'$  formed via spinodal decomposition from the supersaturated  $\gamma$  matrix at subsolvus temperatures [72,73]. The rapid formation of early-stage nanoscale  $\gamma'$  during short-time heating significantly enhances the overall strength. This effect has been demonstrated in ABD-900AM [74] and IN738LC [48], where a clear microhardness increase was observed after 60 s at intermediate temperatures (e.g., 727 °C and 850 °C), confirming the pronounced strengthening contribution of nano- $\gamma'$  phase.

During heating from the as-built condition,  $\gamma'$  formation is also associated with the decreasing of its lattice parameter, which introduces a transformation-induced stress under constrained expansion conditions, on the order of ~60–105 MPa between 550 °C and 700 °C, as quantified by Markanday et al. [25]. Forsik et al. [75] tailored the chemical composition to maintain a positive  $\gamma/\gamma'$  lattice misfit across the SAC temperature range, thereby reducing transformation-induced stress in Ni and Co-Ni high- $\gamma'$  superalloys to mitigate SAC. However,

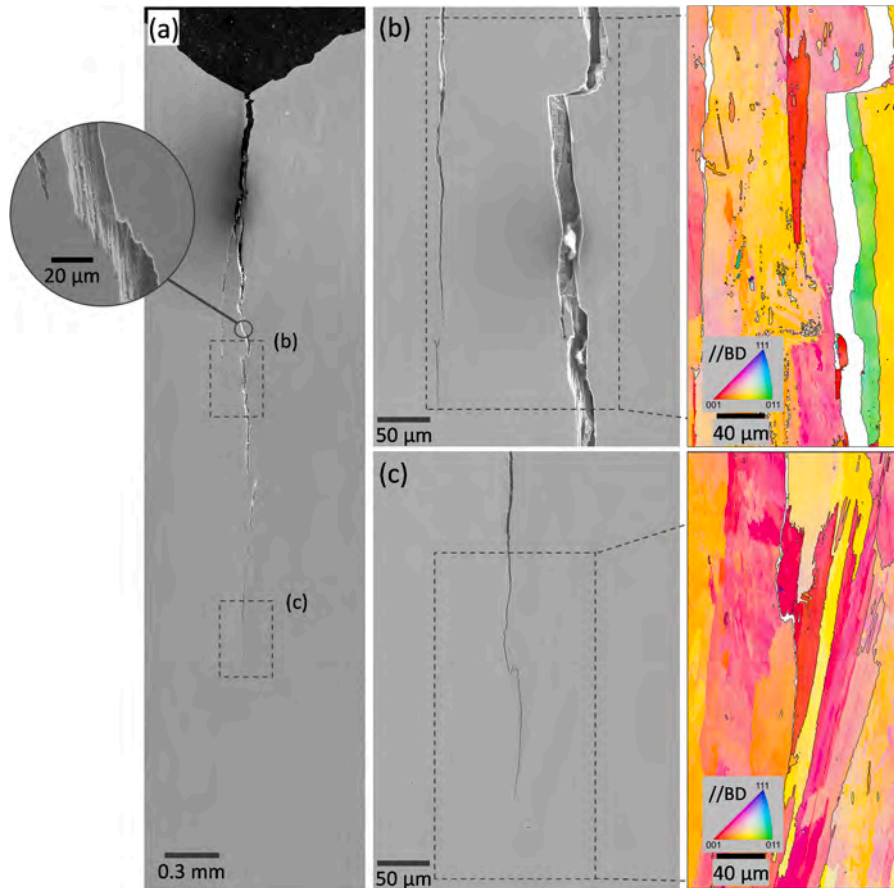
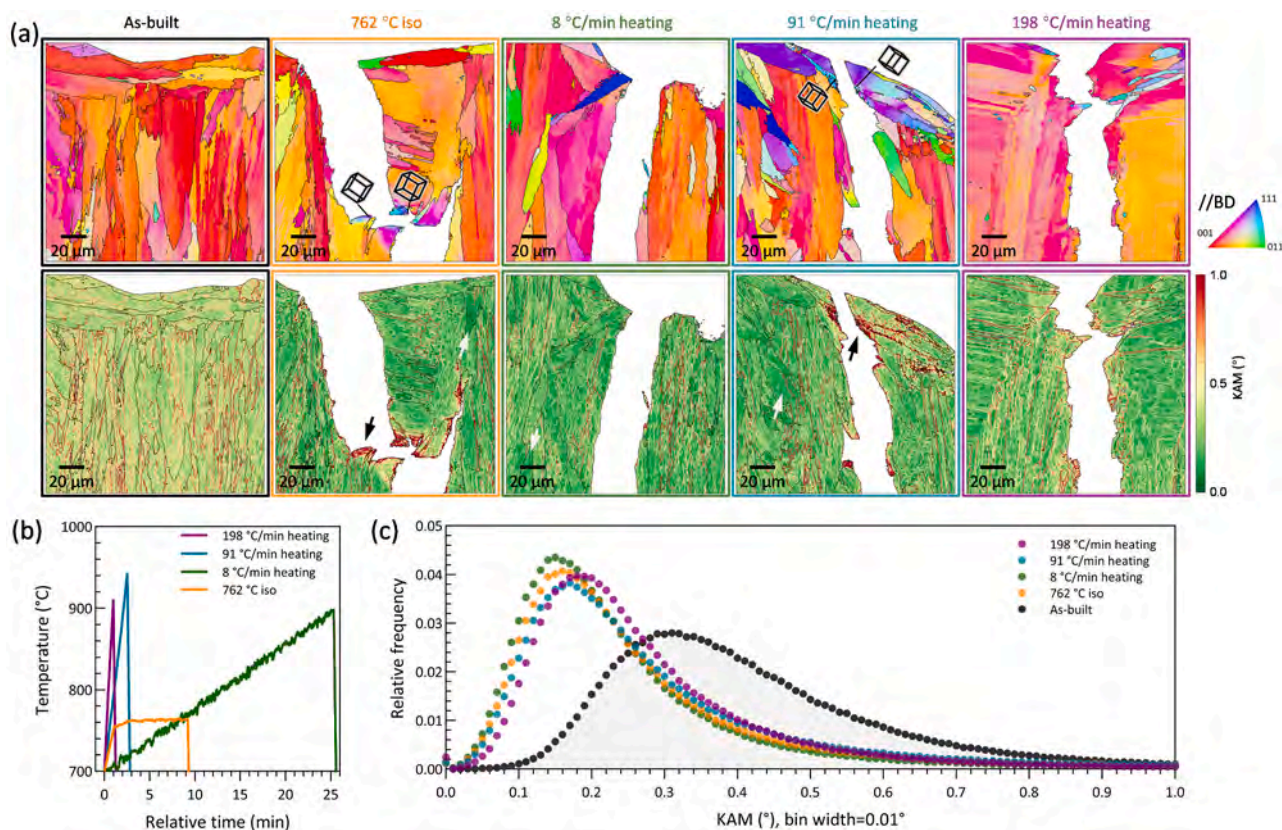


Fig. 14. Cross-sectional view of the SAC morphology in a  $d = 2$  mm notch sample with minimal oxidation, achieved via induction heating at 200 °C/min to 900 °C. (a) Stitched secondary electron micrograph of the as-polished surface, with an inset showing the SAC morphology, (b) enlarged view of the mid-section of the SAC, (c) enlarged view of the SAC tip together with their IPF coloring maps from EBSD scans.



**Fig. 15.** EBSD analysis of SAC initiation sites: (a) IPF coloring maps and KAM maps of regions close to notch tip of as-built, and SACed samples of 762 °C isothermal, 8 °C/min, 91 °C/min, and 198 °C/min heating conditions. All the EBSD scans were done at the identical magnification and step size (0.2 μm), (b) heating curves of the SACed samples showing the thermal history, and (c) histogram comparing the KAM distributions. Bin width = 0.01°.

transformation stress alone does not correlate with SAC susceptibility across the alloys investigated by Markanday et al. [25], where an alloy exhibiting lower SAC susceptibility displayed higher precipitation-induced stresses. This indicates that volumetric transformation strain may not be the dominant factor controlling SAC initiation.

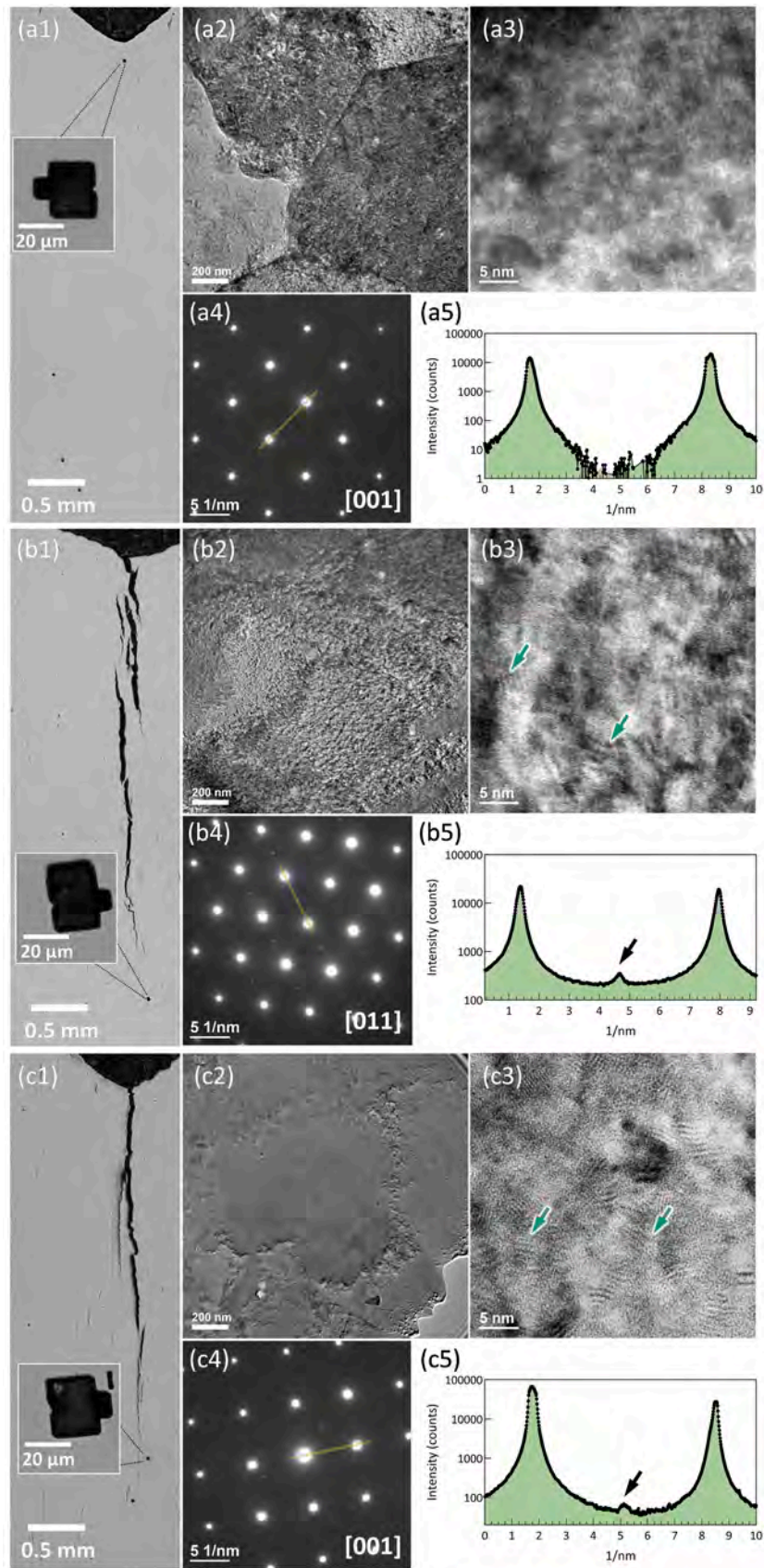
On the other hand, superalloys are known to exhibit a ductility dip at intermediate temperatures. However, such ductility measurements are typically conducted under stabilized microstructures following post-processing heat treatments [4,76]. In contrast, SAC occurs under continuously evolving microstructural conditions during heating. A plausible mechanism for SAC initiation is that the rapid formation of early nanoscale  $\gamma'$  leads to localized ductility reduction. As coherent nano- $\gamma'$  dispersions strengthen within the grain interior (as shown by HRTEM in Fig. 16), and very likely also strengthen grain boundaries due to enrichment of  $\gamma'$ -forming elements, the effective ductile volume is reduced and strain accommodation becomes increasingly restricted. Under residual stresses and in the absence of external loading, stress redistribution is therefore concentrated toward grain boundaries, where strain accommodation capability is limited, promoting localized intergranular cracking. For PBF-LB IN738LC, a correlation between increased grain interior hardness (measured by nanoindentation) and intergranular cracking has been demonstrated [10]. However, direct experimental evidence linking transient nano- $\gamma'$  formation during heating to localized ductility reduction remains limited.

The onset temperature depends on the heating rate under continuous heating and on the hold temperature under isothermal conditions, reflecting the kinetics of  $\gamma'$  precipitation (Fig. 9). Because  $\gamma'$  precipitation is largely suppressed in the as-built microstructure, the first  $\gamma'$  population forms during the initial heating cycle, with the commencement temperature shifting with heating rate. For example, in PBF-LB ABD-900AM

superalloy, increasing the heating rate from 6 to 6000 °C/min delayed  $\gamma'$  nucleation from 461 to 579 °C [44]. For PBF-LB IN738LC,  $\gamma'$  formation was observed at ~525 °C at 300 °C/min, based on electrical resistance measurements [77]. However, the  $\gamma'$  formation temperature is not necessarily the same as the SAC onset temperature which was found to be >300 °C higher in the equivalent heating rate in this study. In addition, as a rough comparison with ignoring residual stress, in  $\gamma'$ -containing microstructures such as welded IN738LC joints, SAC has been reported between 700 and 1000 °C during post-weld heat treatment [78]. Thus, no decrement of SAC onset temperature can be concluded for the PBF-LB condition attributed to the lower  $\gamma'$  precipitation commencement temperature.

During the SAC propagation regime, residual stress from the PBF-LB process provides the primary driving force for crack growth (shown in the notch depth dependence of SAC growth rate in Fig. 8 (cont.1)). In addition, transverse stresses generated by oxide scale growth on both sides of the crack surface act as a wedge, mechanically assisting crack opening. Oxide wedging can promote crack advance through volumetric expansion associated with oxide formation along grain boundaries, which generates compressive stresses within the oxide scale along the crack flanks [79]. In the SAC propagation regime where no external mechanical load is applied (comparable to the unstressed condition reported by Kitaguchi et al. [80]), oxide wedging plays a significant role, as indicated by the deep oxidation intrusions observed ahead of the crack tip.

The crack advances from the notch tip inward, with each segment exposed to ambient air at different times. For IN738LC, oxidation typically develops in an outer-to-inner sequence of TiO<sub>2</sub>-Cr<sub>2</sub>O<sub>3</sub>-internal Al oxidation [81–83]. The growth of oxides creates significant volumetric deformation, considering the Pilling and Bedworth ratio (PBR) of Cr<sub>2</sub>O<sub>3</sub> in NiCr system as 2.42 [84] which is well exceeding 1. The growth of



(caption on next page)

**Fig. 16.** TEM characterization of the as-built and SACed samples obtained after 198 °C/min rapid heating and 762 °C isothermal conditions. Optical micrographs showing the locations of TEM lamella extraction are presented in (a1) as-built, (b1) rapid heating, and (c1) isothermal samples. Bright-field TEM images are shown in (a2) as-built, (b2) rapid heating, and (c2) isothermal conditions. The corresponding high-resolution TEM (HRTEM) images are shown in (a3) as-built, (b3) rapid heating, and (c3) isothermal conditions, where local lattice distortions are indicated by arrows. Electron diffraction patterns are presented in (a4) as-built along the [001] zone axis, (b4) rapid heating along the [011] zone axis, and (c4) isothermal conditions along the [001] zone axis. The corresponding intensity profiles extracted along the highlighted lines in the diffraction patterns are shown in (a5), (b5), and (c5), respectively.

compacted Cr-rich oxides from both sides of SAC is observed in Fig. 12 (c). At the crack tip (Fig. 12(d)), the existence of only Al- and Ti- oxides is likely owing to the reduced oxygen partial pressure ahead of the crack [85], given the fact that equilibrium partial pressures at 1100°C for Cr<sub>2</sub>O<sub>3</sub> is 6 and 11 order of magnitudes greater than TiO<sub>2</sub> and Al<sub>2</sub>O<sub>3</sub>, respectively [86]. On the other hand, it should also be noted that under cyclic loading conditions, oxide-induced loading is primarily displacement-controlled. As a result, the effective stress intensity range factor may remain approximately constant or reduced, which can suppress additional fatigue crack growth while oxide wedging remains active [87,88]. However, the quantitative contribution of oxide wedging to the effective crack-driving force during SAC propagation remains unclear and needs further investigation. Then the  $\gamma'$ -depleted zone observed at the SAC and notch tips, in both SACed and non-SACed samples, arises from the outward interdiffusion of  $\gamma'$ -forming elements to sustain oxide formation. A schematic summary of the SAC behavior in V-notch PBF-LB IN738LC is presented in Fig. 17.

#### 4.2. SAC susceptibility of superalloys

To genericize the chemical composition-dependent susceptibility to SAC in various nickel-based superalloys produced by PBF-LB, different methods have been developed. For example, a SAC index,  $M_{SAC}$ , was proposed to assess the likelihood of SAC expressed as  $M_{SAC} = Al \text{ (wt.\%)} + 0.5 \times Ti \text{ (wt.\%)} + 0.3 \times Nb \text{ (wt.\%)} + 0.15 \times Ta \text{ (wt.\%)}$ , which considers  $\gamma'$  formers like Nb and Ta having less significant per unit weight compared to Al and Ti by assigning them smaller weighting factors [3]. The  $M_{SAC}$  is a simplified and easy-to-use index that corresponds well to

the equilibrium amount of  $\gamma'$ . As reported in the validation by Chechik et al. [89], not surprisingly, the predicted equilibrium  $\gamma'$  volume fraction and the  $M_{SAC}$  shows a strong positive correlation in a linear regression. A heuristically-chosen criterion of  $M_{SAC} = 4 \text{ wt.\%}$  was set as the upper limit for alloys that would have high SAC susceptibility based on the experience that SAC was reported in high  $\gamma'$  containing alloys like IN738LC [90] and CM247LC [91], while SAC is absent for lower  $\gamma'$  containing alloys like IN939 [92].

Specifically, we emphasize that SAC initiation occurs during early-stage nanoscale  $\gamma'$  formation, when the  $\gamma'$  fraction remains far below its equilibrium value. Therefore, SAC susceptibility in this context is governed primarily by  $\gamma'$  formation kinetics rather than equilibrium  $\gamma'$  content, although correlations between the kinetics and equilibrium  $\gamma'$  fraction may exist. Besides the index that quantifies the tendency of  $\gamma'$  formation like  $M_{SAC}$ , some other index that describes the kinetics of  $\gamma'$  precipitation is likely to be useful to assess the SAC susceptibility. Yu et al. [93,94] proposed a SAC criterion based on calculation of the derivative of volume fraction of  $\gamma$  matrix with respect to temperature in a critical temperature range between the temperature when matrix  $\gamma$  phase reaches 80% and the solidus temperature. This SAC criterion shows that a wide range of homogenization microstructure and a gradual change in precipitation volume with temperature will ensure as high threshold strain rate for crack formation, which will accordingly result in the low tendency of strain-age cracks, and vice versa [95,96].

Owing to the fast kinetics of  $\gamma'$  precipitation, for example, from the simulated TTT diagrams [97], 0.5%  $\gamma'$  formed within 1 s and 2 s for CM247LC and IN738LC, respectively, at their corresponding “nose” temperature. Such quick precipitation behavior indicates no feasible

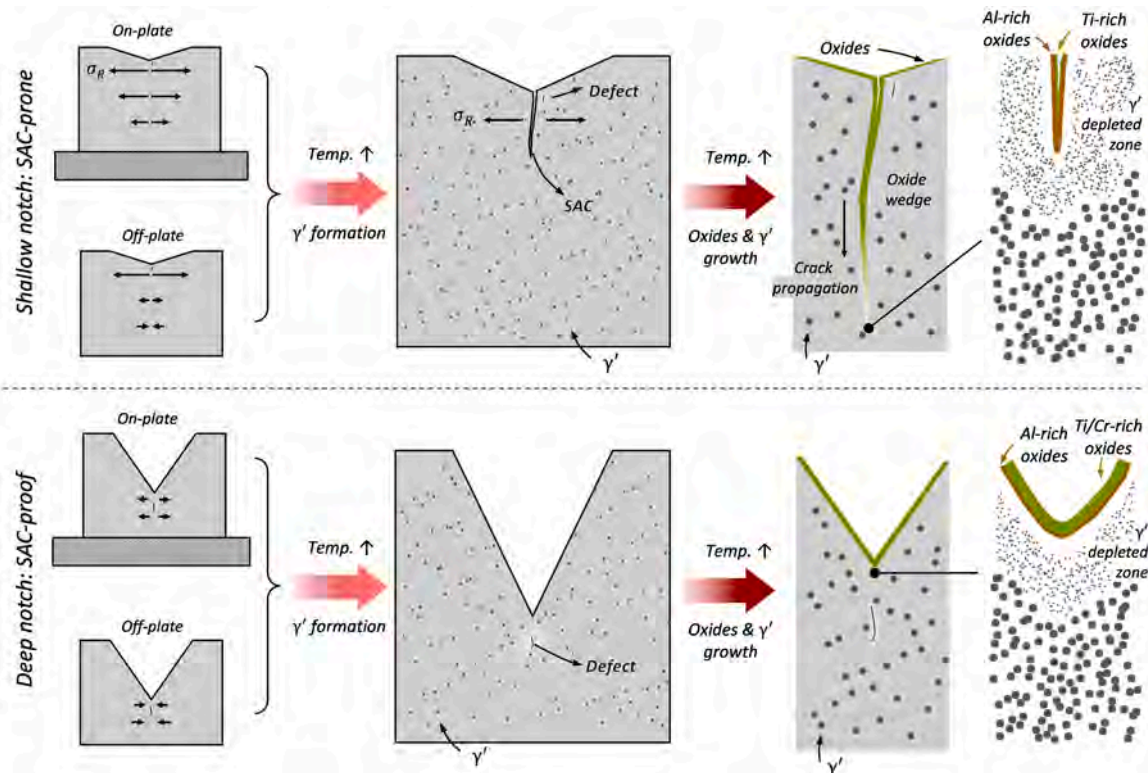


**Fig. 17.** Schematic comparison of SAC-prone and SAC-resistant V-notches in PBF-LB IN738LC samples.

rapid heating methods are applicable to bypass the SAC susceptible region as suggested by the SAC susceptibility diagram in Fig. 9 with the highest heating rate up to approximately 1000 °C/min. Reducing the alloys  $\gamma'$  volume fraction or reaching the  $\gamma'$  solvus temperature without significant  $\gamma'$  formation may not be the only methods to avoid SAC.

## 5. Conclusion

The present work investigated SAC in a PBF-LB processed  $\gamma'$ -strengthened nickel-based superalloy IN738LC using V-notch samples subjected to various heating conditions. The following conclusions can be drawn:

1. SAC initiation follows  $\gamma'$  precipitation kinetics, with onset temperatures corresponding closely to the precipitation of  $\gamma'$  on a TTT diagram. Under continuous heating, faster heating rates shift the measured SAC onset to higher temperatures, indicating that the onset temperature is a kinetic indicator rather than a unique thermodynamic threshold. Under isothermal conditions, SAC still occurs after sufficient incubation time, with lower temperatures requiring longer holding times to initiate cracking.
2. TEM analysis confirms the emergence of nanoscale  $\gamma'$  in SACed samples under both rapid heating and isothermal conditions, suggesting that SAC initiation is governed by nanoscale  $\gamma'$ -induced strengthening and localized ductility reduction.
3. Residual stress governs SAC growth rate rather than onset temperature. Shallow notches, with higher tensile stresses near the notch tip, exhibit rapid SAC propagation whereas deeper notches remain largely crack-free due to stress relaxation.
4. SAC propagates predominantly along grain boundaries. Occasional transgranular cracking occurs under rapid crack growth, accompanied by localized plastic deformation.
5. SAC propagation is further assisted by wedge-shaped intrusions of oxides. Most stored energy is released prior to SAC initiation, particularly under fast heating, indicating that SAC results from instability of local ductility deficit rather than serving as a stress-relief mechanism.

### Declaration of generative AI and AI-assisted technologies in the writing process

During the preparation of this work the author(s) used ChatGPT-4o/ChatGPT-5 to check grammar and improve readability. After using this

### Supplementary materials

Supplementary material associated with this article can be found, in the online version, at [doi:10.1016/j.actamat.2026.122244](https://doi.org/10.1016/j.actamat.2026.122244).

### Appendix

Mean pixel intensity in the beam-center region (425 px  $\times$  425 px ROI) plotted as a function of distance from the notch tip.

tool/service, the author(s) reviewed and edited the content as needed and take(s) full responsibility for the content of the publication.

### Data availability

Data will be made available on request.

### CRediT authorship contribution statement

**Jinghao Xu:** Writing – review & editing, Writing – original draft, Visualization, Validation, Software, Methodology, Investigation, Formal analysis, Data curation, Conceptualization. **Abdul Shaafi Shaikh:** Writing – review & editing, Validation, Methodology, Investigation. **Henry Boyle:** Writing – review & editing, Software, Methodology, Investigation, Data curation. **Sofia Kazi:** Writing – original draft, Software, Methodology, Investigation, Formal analysis, Data curation. **Justinas Palisaitis:** Formal analysis, Investigation, Methodology, Writing – review & editing. **Ru Lin Peng:** Writing – review & editing, Methodology, Investigation, Formal analysis, Data curation. **Eduard Hryha:** Resources, Funding acquisition. **Johan Moverare:** Writing – review & editing, Resources, Funding acquisition.

### Declaration of competing interest

The authors declare that they have no known competing financial interests or personal relationships that could have appeared to influence the work reported in this paper.

### Acknowledgement

This work has been performed with support from the Swedish Governmental Agency for Innovation Systems, (Vinnova grant 2021–01005 (MAGDA) and 2024–02716 (TILDA)). Centre for Additive Manufacturing – Metal (CAM<sup>2</sup>) is acknowledged. The authors would also like to acknowledge Tijmen Jacobs from the Department of Physics at Chalmers for assisting in experiments performed at PETRA III, DESY. Competence Centre NEutron and X-ray science for industrial Technology transitions (NEXT, Vinnova grant 2023–00553) is acknowledged. Swedish Research Council and Swedish Foundation for Strategic Research acknowledged for access to ARTEMI, the Swedish National Infrastructure in Advanced Electron Microscopy (2021–00171 and RIF21-0026).

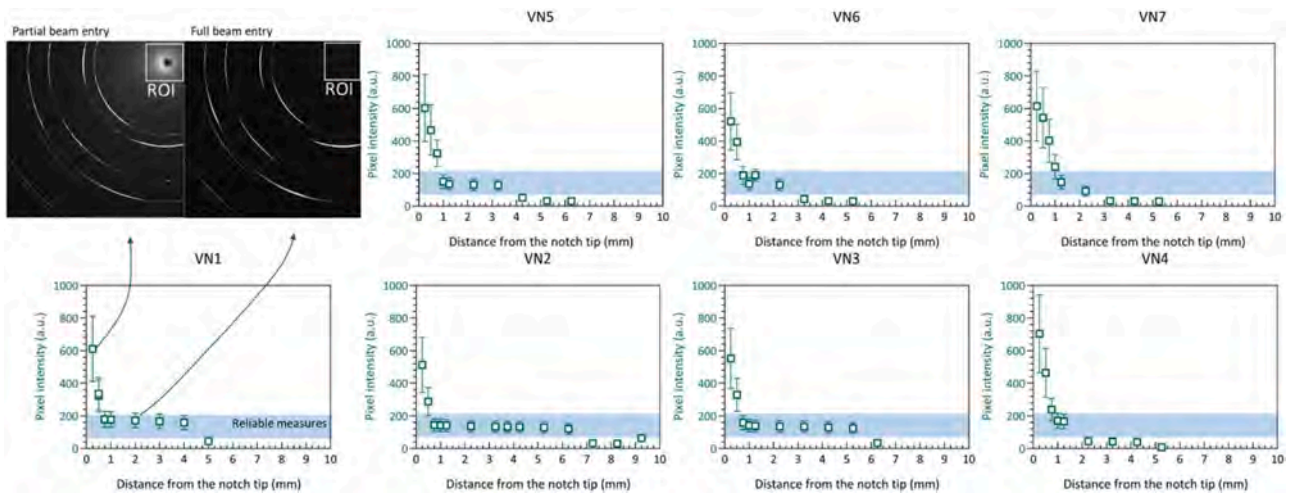


Fig. A1. Mean pixel intensity in the direct-beam region of interest on the 2D detector, plotted as a function of distance from the notch tip. The insets show diffraction images illustrating partial versus full beam entry into the sample.

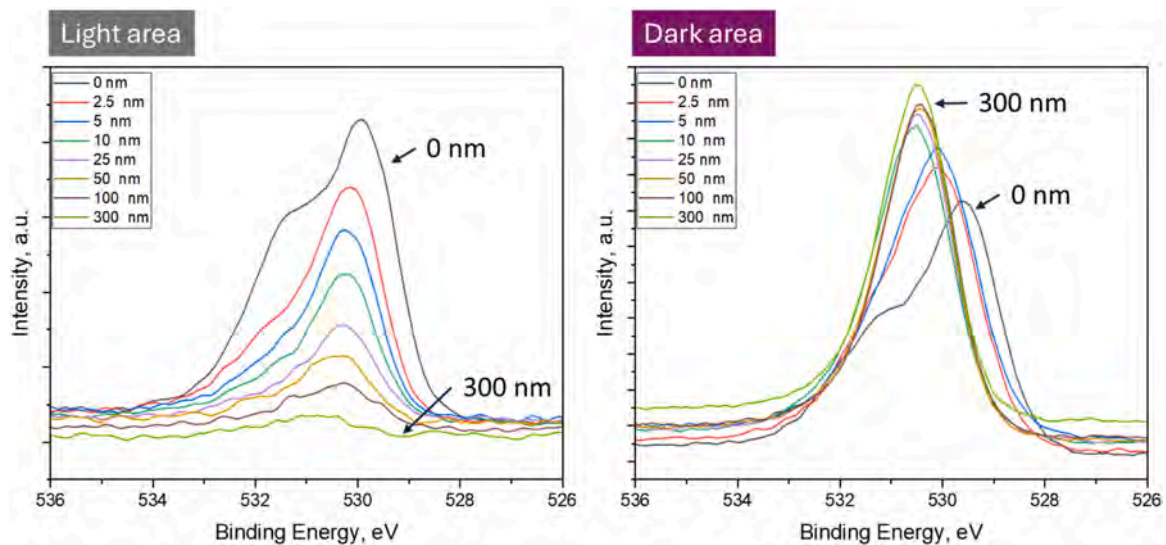


Fig. A2. XPS depth profile of O 1s region from light and dark area on SAC fractures after 1120 °C/2 h heat treatment.

## References

- [1] J.C. Lippold, *Welding Metallurgy and Weldability*, Wiley, 2014, <https://doi.org/10.1002/9781118960332>.
- [2] J. Xu, P. Kontis, R.L. Peng, J. Moverare, Modelling of additive manufacturability of nickel-based superalloys for laser powder bed fusion, *Acta Mater.* 240 (2022) 118307, <https://doi.org/10.1016/j.actamat.2022.118307>.
- [3] Y.T. Tang, C. Panwisawas, J.N. Ghossoub, Y. Gong, J. Clark, A. Németh, D. G. McCartney, R.C. Reed, Alloys-by-design: application to new superalloys for additive manufacturing, *Acta Mater.* (2020), <https://doi.org/10.1016/j.actamat.2020.09.023>.
- [4] N. Zhou, A.D. Dicus, S.A.J. Forsik, T. Wang, G.A. Colombo, M.E. Epler, Development of a new alumina-forming crack-resistant high- $\gamma'$  fraction Ni-base superalloy for additive manufacturing, *TMS Superalloys 2020* (2020) 1046–1054, [https://doi.org/10.1007/978-3-030-51834-9\\_102](https://doi.org/10.1007/978-3-030-51834-9_102).
- [5] J.N. Ghossoub, Y.T. Tang, C. Panwisawas, A. Németh, R.C. Reed, On the influence of alloy chemistry and processing conditions on additive manufacturability of Ni-based superalloys, in: *superalloys 2020*, *Miner. Met. Mater. Ser.* (2020) 153–162, [https://doi.org/10.1007/978-3-030-51834-9\\_15](https://doi.org/10.1007/978-3-030-51834-9_15).
- [6] H. Hilal, R. Lancaster, S. Jeffs, J. Boswell, D. Stapleton, G. Baxter, The influence of process parameters and build orientation on the creep behaviour of a laser powder bed fused Ni-based superalloy for aerospace applications, *Materials* 12 (2019) 1390, <https://doi.org/10.3390/ma12091390>.
- [7] Y.T. Tang, J.N. Ghossoub, C. Panwisawas, D.M. Collins, S. Amirkhanlou, J.W. G. Clark, A.A.N. Németh, D. McCartney, R.C. Reed, The effect of heat treatment on tensile yielding response of the new superalloy ABD-900AM for additive manufacturing, *Miner. Met. Mater. Ser.* (2020) 1055–1065, [https://doi.org/10.1007/978-3-030-51834-9\\_103](https://doi.org/10.1007/978-3-030-51834-9_103).
- [8] A.S. Shaikh, F. Schulz, K. Minet-Lallemand, E. Hryha, Microstructure and mechanical properties of Haynes 282 superalloy produced by laser powder bed fusion, *Mater. Today Commun.* 26 (2021) 102038, <https://doi.org/10.1016/j.mtcomm.2021.102038>.
- [9] J. Xu, H. Gruber, R. Peng, J. Moverare, A novel  $\gamma'$ -strengthened nickel-based superalloy for laser powder bed fusion, *Materials* 13 (2020) 4930, <https://doi.org/10.3390/ma13214930>.
- [10] J. Xu, H. Gruber, R. Boyd, S. Jiang, R.L. Peng, J.J. Moverare, On the strengthening and embrittlement mechanisms of an additively manufactured Nickel-base superalloy, *Materialia* 10 (2020) 100657, <https://doi.org/10.1016/j.mtla.2020.100657>.
- [11] J.R. Miller, J.F.S. Markanday, S.M. Fairclough, G.J. Wise, C.M.F. Rae, L.R. Owen, D. Stapleton, N. D'Souza, P.A.J. Bagot, H.J. Stone, Gamma prime precipitation in as-deposited Ni-based superalloy IN713LC, *Scr. Mater.* 239 (2024) 115775, <https://doi.org/10.1016/j.scriptamat.2023.115775>.
- [12] X. Wang, L.N. Carter, B. Pang, M.M. Attallah, M.H. Loretto, Microstructure and yield strength of SLM-fabricated CM247LC Ni-Superalloy, *Acta Mater.* 128 (2017) 87–95, <https://doi.org/10.1016/j.actamat.2017.02.007>.
- [13] J.O. Aina, O.A. Ojo, M.C. Chaturvedi, Enhanced laser weldability of an aerospace superalloy by thermal treatment, *Sci. Technol. Weld. Join.* 24 (2019) 225–234, <https://doi.org/10.1080/13621718.2018.1518767>.
- [14] J.N. DuPont, J.C. Lippold, S.D. Kiser, J.N. DuPont, J.C. Lippold, S.D. Kiser, *Welding Metallurgy and Weldability of Nickel-Base Alloys*, Wiley, Hoboken, NJ, USA, 2009, <https://doi.org/10.1002/9780470500262>.

- [15] E.A. Jägle, Z. Sheng, L. Wu, L. Lu, J. Risse, A. Weisheit, D. Raabe, Precipitation reactions in age-hardenable alloys during laser additive manufacturing, *JOM* (2016), <https://doi.org/10.1007/s11837-015-1764-2>.
- [16] J.A. Muñoz-Lerma, Y. Tian, X. Wang, R. Gauvin, M. Brochu, Microstructure evolution of Inconel 738 fabricated by pulsed laser powder bed fusion, *Prog. Addit. Manuf.* 4 (2019) 97–107, <https://doi.org/10.1007/s40964-018-0062-2>.
- [17] K. Kunze, T. Etter, J. Grässlin, V. Shklover, Texture, anisotropy in microstructure and mechanical properties of IN738LC alloy processed by selective laser melting (SLM), *Mater. Sci. Eng. A.* 620 (2014) 213–222, <https://doi.org/10.1016/j.msea.2014.10.003>.
- [18] S. Ghosh, L. Ma, N. Ofori-Opoku, J.E. Guyer, On the primary spacing and microsegregation of cellular dendrites in laser deposited Ni–Nb alloys, *Model. Simul. Mater. Sci. Eng.* 25 (2017) 065002, <https://doi.org/10.1088/1361-651X/aa7369>.
- [19] J.M. Vitek, T.J. Fitzgerald, Y/AMT-622 Welding And Weldability of Directionally Solidified Single Crystal Nickel-Base Super-Alloys, 1996.
- [20] J.H. Boswell, D. Clark, W. Li, M.M. Attallah, Cracking during thermal post-processing of laser powder bed fabricated CM247LC Ni-superalloy, *Mater. Des.* 174 (2019) 107793, <https://doi.org/10.1016/j.matdes.2019.107793>.
- [21] F. Uzun, M.F. Slim, H. Basoalto, K. Liogas, Z.I. Wang, A.M. Korsunsky, Application of strain tomography and contour method to residual stress analysis in additively manufactured CM247LC superalloy parts, *Prog. Addit. Manuf.* (2025), <https://doi.org/10.1007/s40964-025-01116-2>.
- [22] M.V.R.S. Jensen, D. Dye, K.E. James, A.M. Korsunsky, S.M. Roberts, R.C. Reed, Residual stresses in a welded superalloy disc: characterization using synchrotron diffraction and numerical process modeling, *Metall. Mater. Trans. A.* 33 (2002) 2921–2931, <https://doi.org/10.1007/s11661-002-0277-0>.
- [23] A. Fardan, A. Fazi, R.L. Peng, T. Mishurova, M. Thuvander, G. Bruno, H. Brodin, E. Hryha, Fine-tuning melt pools and microstructures: taming cracks in powder bed fusion—laser beam of a non-weldable Ni-base superalloy, *Materialia* 34 (2024) 102059, <https://doi.org/10.1016/j.mtla.2024.102059>.
- [24] A. Fardan, A. Fazi, J. Schröder, T. Mishurova, T. Deckers, G. Bruno, M. Thuvander, A. Markström, H. Brodin, E. Hryha, Microstructure tailoring for crack mitigation in CM247LC manufactured by powder bed fusion – Laser beam, *Addit. Manuf.* 99 (2025) 104672, <https://doi.org/10.1016/j.addma.2025.104672>.
- [25] J.F.S. Markanday, N. D'Souza, N.L. Church, J.R. Miller, J.J.C. Pitchforth, L.D. Connor, S. Michalik, B. Roebuck, N.G. Jones, K.A. Christofidou, H.J. Stone, The relationship between strain-age cracking and the evolution of  $\gamma'$  in laser powder-bed-fusion processed Ni-based superalloys, in: 2024: pp. 822–835. doi:10.1007/978-3-031-63937-1\_77.
- [26] K. Dörries, C. Haberland, J. Burow, J. Rösler, B. Gehrman, C. Somsen, S. Piegert, H. Brodin, Beyond hot cracking: impact of minor elements on a novel Ni-based superalloy for additive manufacturing, in: 2024: pp. 871–882. doi:10.1007/978-3-031-63937-1\_81.
- [27] R.A. Stevens, P.E.J. Flewitt, Intermediate regenerative heat treatments for extending the creep life of the superalloy IN-738, *Mater. Sci. Eng.* 50 (1981) 271–284, [https://doi.org/10.1016/0025-5416\(81\)90186-5](https://doi.org/10.1016/0025-5416(81)90186-5).
- [28] N. El-Bagoury, M. Waly, A. Nofal, Effect of various heat treatment conditions on microstructure of cast polycrystalline IN738LC alloy, *Mater. Sci. Eng. A.* 487 (2008) 152–161, <https://doi.org/10.1016/j.msea.2007.10.004>.
- [29] H. Wang, X. Zhang, G.B. Wang, J. Shen, G.Q. Zhang, Y.P. Li, M. Yan, Selective laser melting of the hard-to-weld IN738LC superalloy: efforts to mitigate defects and the resultant microstructural and mechanical properties, *J. Alloys. Compd.* 807 (2019) 151662, <https://doi.org/10.1016/j.jallcom.2019.151662>.
- [30] F. Geiger, K. Kunze, T. Etter, Tailoring the texture of IN738LC processed by selective laser melting (SLM) by specific scanning strategies, *Mater. Sci. Eng. A.* 661 (2016) 240–246, <https://doi.org/10.1016/j.msea.2016.03.036>.
- [31] J. Schindelin, I. Arganda-Carreras, E. Frise, V. Kaynig, M. Longair, T. Pietzsch, S. Preibisch, C. Rueden, S. Saalfeld, B. Schmid, J.-Y. Tinevez, D.J. White, V. Hartenstein, K. Eliceiri, P. Tomancak, A. Cardona, Fiji: an open-source platform for biological-image analysis, *Nat. Methods* 9 (2012) 676–682, <https://doi.org/10.1038/nmeth.2019>.
- [32] D. Deng, R.L. Peng, J. Moverare, A comparison study of the dwell-fatigue behaviours of additive and conventional IN718: the role of dislocation substructure on the cracking behaviour, *Mater. Sci. Eng. A.* 797 (2020) 140072, <https://doi.org/10.1016/j.msea.2020.140072>.
- [33] D. Grange, A. Queva, G. Guillemot, M. Bellet, J.-D. Bartout, C. Colin, Effect of processing parameters during the laser beam melting of Inconel 738: comparison between simulated and experimental melt pool shape, *J. Mater. Process. Technol.* 289 (2021) 116897, <https://doi.org/10.1016/j.jmatprotec.2020.116897>.
- [34] W. Zhou, Y. Tian, Q. Tan, S. Qiao, H. Luo, G. Zhu, D. Shu, B. Sun, Effect of carbon content on the microstructure, tensile properties and cracking susceptibility of IN738 superalloy processed by laser powder bed fusion, *Addit. Manuf.* 58 (2022) 103016, <https://doi.org/10.1016/j.addma.2022.103016>.
- [35] J. Risse, Additive Manufacturing of Nickel-Base Superalloy IN738LC by Laser Powder Bed Fusion, RWTH Aachen University, 2019, <https://doi.org/10.18154/RWTH-2019-06822>.
- [36] M. Kusano, T. Osada, M. Watanabe, Data-driven optimization of laser scanning conditions in laser powder bed fusion for defect-free IN738LC components, *J. Manuf. Process.* 151 (2025) 354–371, <https://doi.org/10.1016/j.jmapro.2025.07.023>.
- [37] L. Rickenbacher, T. Etter, S. Hövel, K. Wegener, High temperature material properties of IN738LC processed by selective laser melting (SLM) technology, *Rapid Prototyp. Journal* 19 (2013) 282–290, <https://doi.org/10.1108/13552541311323281>.
- [38] J. Chen, J. Xu, J. Moverare, L.A. Barrales-Mora, Effect of the building direction on the high-temperature mechanical properties of an IN738LC superalloy processed by laser-powder bed fusion, *Mater. Sci. Eng. A.* 909 (2024) 146756, <https://doi.org/10.1016/j.msea.2024.146756>.
- [39] E. Uhlmann, E. Krohmer, F. Schmeiser, N. Schell, W. Reimers, A laser powder bed fusion system for in situ x-ray diffraction with high-energy synchrotron radiation, *Rev. Sci. Instrum.* 91 (2020), <https://doi.org/10.1063/1.5143766>.
- [40] F. Schmeiser, E. Krohmer, N. Schell, E. Uhlmann, W. Reimers, Experimental observation of stress formation during selective laser melting using in situ X-ray diffraction, *Addit. Manuf.* 32 (2020), <https://doi.org/10.1016/j.addma.2019.101028>.
- [41] M. Newville, T. Stensitzki, D.B. Allen, M. Rawlik, A. Ingarciola, A. Nelson, LMFIT: non-linear least-square minimization and curve-fitting for Python, *Astrophys. Source Code Libr.* (2016), <https://doi.org/10.5281/zenodo.15014437> ascl-1606.
- [42] M. Moreno, J.M. Andersson, J. Eriksson, P. Alm, K. Hedström, R. M'Saoubi, I. C. Schramm, N. Schell, M.P. Johansson-Joësaar, M. Odén, L. Rogström, Strain and phase evolution in TiAlN coatings during high-speed metal cutting: an in operando high-energy x-ray diffraction study, *Acta Mater.* 263 (2024) 119538, <https://doi.org/10.1016/j.actamat.2023.119538>.
- [43] U. Bayerlein, H.G. Sockel, Determination of single crystal elastic constants from DS- and DR-Ni-based superalloys by a new regression method between 20 °C and 1200 °C, in: *Superalloys 1992* (Seventh International Symposium, TMS, 1992), pp. 695–704, [https://doi.org/10.7449/1992/Superalloys\\_1992\\_695\\_704](https://doi.org/10.7449/1992/Superalloys_1992_695_704).
- [44] Y.T. Tang, C. Panwisawas, B.M. Jenkins, J. Liu, Z. Shen, E. Salvati, Y. Gong, J. N. Ghousoub, S. Michalik, B. Roebuck, P.A.J. Bagot, S. Lozano-Perez, C.R. M. Grovenor, M.P. Moody, A.M. Korsunsky, D.M. Collins, R.C. Reed, Multi-length-scale study on the heat treatment response to supersaturated nickel-based superalloys: precipitation reactions and incipient recrystallisation, *Addit. Manuf.* 62 (2023) 103389, <https://doi.org/10.1016/j.addma.2023.103389>.
- [45] D. Ershov, M.-S. Phan, J.W. Pylvänäinen, S.U. Rigaud, L. Blanc, A. Charles-Orszag, J.R.W. Conway, R.F. Laine, N.H. Roy, D. Bonazzi, G. Duménil, G. Jacquemet, J.-Y. Tinevez, TrackMate 7: integrating state-of-the-art segmentation algorithms into tracking pipelines, *Nat. Methods* 19 (2022) 829–832, <https://doi.org/10.1038/s41592-022-01507-1>.
- [46] J.-Y. Tinevez, N. Perry, J. Schindelin, G.M. Hoopes, G.D. Reynolds, E. Laplantine, S. Y. Bednarek, S.L. Shorte, K.W. Eliceiri, TrackMate: an open and extensible platform for single-particle tracking, *Methods* 115 (2017) 80–90, <https://doi.org/10.1016/j.ymeth.2016.09.016>.
- [47] G. Farneback, Two-frame motion estimation based on polynomial expansion, in: 2003: pp. 363–370. doi:10.1007/3-540-45103-X\_50.
- [48] F. Schulz, K. Lindgren, J. Xu, E. Hryha, Gamma prime formation in nickel-based superalloy IN738LC manufactured by laser powder bed fusion, *Mater. Today Commun.* 38 (2024) 107905, <https://doi.org/10.1016/j.mtcomm.2023.107905>.
- [49] W.P. Hughes, T.F. Berry, R.E. Yount, A study of the strain-age crack sensitivity of Rene' 41, 1968.
- [50] J. Xu, H. Gruber, D. Deng, R.L. Peng, J.J. Moverare, Short-term creep behavior of an additive manufactured non-weldable Nickel-base superalloy evaluated by slow strain rate testing, *Acta Mater.* 179 (2019) 142–157, <https://doi.org/10.1016/j.actamat.2019.08.034>.
- [51] A. Bumajdad, S. Al-Ghareeb, M. Madkour, F. Al Sagheer, Non-noble, efficient catalyst of unsupported  $\alpha$ -Cr2O3 nanoparticles for low temperature CO oxidation, *Sci. Rep.* 7 (2017) 14788, <https://doi.org/10.1038/s41598-017-14779-x>.
- [52] G. Chavez-Esquivel, J.C. García-Martínez, J.A. de los Reyes, V.A. Suárez-Toriello, M.A. Vera-Ramírez, L. Huerta, The influence of Al 2 O 3 content on Al 2 O 3 -ZrO 2 composite-textural structural and morphological studies, *Mater. Res. Express.* 6 (2019) 105201, <https://doi.org/10.1088/2053-1591/ab352d>.
- [53] A. Hariharan, L. Lu, J. Risse, A. Kostka, B. Gault, E.A. Jägle, D. Raabe, Misorientation-dependent solute enrichment at interfaces and its contribution to defect formation mechanisms during laser additive manufacturing of superalloys, *Phys. Rev. Mater.* 3 (2019) 123602, <https://doi.org/10.1103/PhysRevMaterials.3.123602>.
- [54] D. Grange, J.D. Bartout, B. Macquaire, C. Colin, Processing a non-weldable nickel-base superalloy by Selective Laser Melting: role of the shape and size of the melt pools on solidification cracking, *Materialia* 12 (2020) 100686, <https://doi.org/10.1016/j.mtla.2020.100686>.
- [55] P. Hu, Z. Liu, M. Chen, Y. Li, X. Qi, J. Xie, Reducing cracking sensitivity of CM247LC processed via laser powder bed fusion through composition modification, *J. Mater. Res. Technol.* 29 (2024) 3074–3088, <https://doi.org/10.1016/j.jmrt.2024.02.082>.
- [56] J. Xu, H. Brodin, R.L. Peng, V. Luzin, J. Moverare, Effect of heat treatment temperature on the microstructural evolution of CM247LC superalloy by laser powder bed fusion, *Mater. Charact.* 185 (2022) 111742, <https://doi.org/10.1016/j.matchar.2022.111742>.
- [57] K. An, L. Yuan, L. Dial, I. Spinelli, A.D. Stoica, Y. Gao, Neutron residual stress measurement and numerical modeling in a curved thin-walled structure by laser powder bed fusion additive manufacturing, *Mater. Des.* 135 (2017) 122–132, <https://doi.org/10.1016/j.matdes.2017.09.018>.
- [58] C. Li, Z.Y. Liu, X.Y. Fang, Y.B. Guo, On the simulation scalability of predicting residual stress and distortion in selective laser melting, *J. Manuf. Sci. Eng.* 140 (2018), <https://doi.org/10.1115/1.4038893>.
- [59] E.R. Denlinger, J.C. Heigel, P. Michaleris, T.A. Palmer, Effect of inter-layer dwell time on distortion and residual stress in additive manufacturing of titanium and nickel alloys, *J. Mater. Process. Technol.* 215 (2015) 123–131, <https://doi.org/10.1016/j.jmatprotec.2014.07.030>.
- [60] A.S. Wu, D.W. Brown, M. Kumar, G.F. Gallegos, W.E. King, An experimental investigation into additive manufacturing-induced residual stresses in 316L

- stainless steel, *Metall. Mater. Trans. A* 45 (2014) 6260–6270, <https://doi.org/10.1007/s11661-014-2549-x>.
- [61] W.L. Smith, J.D. Roehling, M. Strantz, R.K. Ganeriwala, A.S. Ashby, B. Vrancken, B. Clausen, G.M. Guss, D.W. Brown, J.T. McKeown, M.R. Hill, M.J. Matthews, Residual stress analysis of in situ surface layer heating effects on laser powder bed fusion of 316L stainless steel, *Addit. Manuf.* 47 (2021) 102252, <https://doi.org/10.1016/j.addma.2021.102252>.
- [62] M. Busi, N. Kalentics, M. Morgano, S. Griffiths, A.S. Tremsin, T. Shinohara, R. Logé, C. Leinenbach, M. Strobl, Nondestructive characterization of laser powder bed fusion parts with neutron Bragg edge imaging, *Addit. Manuf.* 39 (2021) 101848, <https://doi.org/10.1016/j.addma.2021.101848>.
- [63] Q. Tan, Y. Liu, Z. Fan, J. Zhang, Y. Yin, M.X. Zhang, Effect of processing parameters on the densification of an additively manufactured 2024 Al alloy, *J. Mater. Sci. Technol.* 58 (2020) 34–45, <https://doi.org/10.1016/j.jmst.2020.03.070>.
- [64] B.X. Cao, D.X. Wei, X.F. Zhang, H.J. Kong, Y.L. Zhao, J.X. Hou, J.H. Luan, Z.B. Jiao, Y. Liu, T. Yang, C.T. Liu, Intermediate temperature embrittlement in a precipitation-hardened high-entropy alloy: the role of heterogeneous strain distribution and environmentally assisted intergranular damage, *Mater. Today Phys.* 24 (2022) 100653, <https://doi.org/10.1016/j.mtphys.2022.100653>.
- [65] A.J. Young, T.E. Capobianco, M.A. Penik, B.W. Morris, *The mechanism of ductility dip cracking in Nickel-chromium alloys*, *Weld. Res.* (2008).
- [66] A.A.N. Németh, D.J. Crudden, D.E.J. Armstrong, D.M. Collins, K. Li, A. J. Wilkinson, C.R.M. Grovenor, R.C. Reed, Environmentally-assisted grain boundary attack as a mechanism of embrittlement in a nickel-based superalloy, *Acta Mater.* 126 (2017) 361–371, <https://doi.org/10.1016/j.actamat.2016.12.039>.
- [67] S.J. Luther, B.T. Alexandrov, S.L. McCracken, J.K. Tatman, Correlation of imposed mechanical energy with ductility-dip cracking in a highly restrained weld of Alloy 52, *J. Manuf. Process.* 79 (2022) 767–788, <https://doi.org/10.1016/j.jmapro.2022.05.027>.
- [68] H. Zhang, W. Song, X. Zhang, J. Liang, Y. Yang, J. Xie, N. Lu, L. Zhou, R. Chen, Y. Zhou, W. Xu, J. Li, Stress rupture behavior of SLM deposited IN738 superalloy via hot isostatic pressing and heat treatment, *Mater. Sci. Eng. A* 946 (2025) 149172, <https://doi.org/10.1016/j.msea.2025.149172>.
- [69] V. Kalyanasundaram, A. De Luca, R. Wróbel, J. Tang, S.R. Holdsworth, C. Leinenbach, E. Hosseini, Tensile and creep-rupture response of additively manufactured nickel-based superalloy CM247LC, *Addit. Manuf. Lett.* 5 (2023) 100119, <https://doi.org/10.1016/j.addlet.2022.100119>.
- [70] A. Fardan, J. Xu, A. Shaafi Shaikh, J. Gårdstam, U. Klement, J. Moverare, H. Brodin, E. Hryha, On the anisotropic creep behavior of a Ni-base superalloy CM247LC manufactured by powder bed fusion – laser beam, *Mater. Sci. Eng. A* 953 (2026) 149707, <https://doi.org/10.1016/j.msea.2025.149707>.
- [71] V.D. Divya, R. Muñoz-Moreno, O.M.D.M. Messé, J.S. Barnard, S. Baker, T. Illston, H.J. Stone, Microstructure of selective laser melted CM247LC nickel-based superalloy and its evolution through heat treatment, *Mater. Charact.* 114 (2016) 62–74, <https://doi.org/10.1016/j.matchar.2016.02.004>.
- [72] G.B. Viswanathan, R. Banerjee, A. Singh, S. Nag, J. Tiley, H.L. Fraser, Precipitation of ordered phases in metallic solid solutions: a synergistic clustering and ordering process, *Scr. Mater.* 65 (2011) 485–488, <https://doi.org/10.1016/j.scriptamat.2011.06.002>.
- [73] D.M. Collins, N. D'Souza, C. Panwisawas, C. Papadaki, G.D. West, A. Kostka, P. Kontis, Spinodal decomposition versus classical  $\gamma'$  nucleation in a nickel-base superalloy powder: an in-situ neutron diffraction and atomic-scale analysis, *Acta Mater.* 200 (2020) 959–970, <https://doi.org/10.1016/j.actamat.2020.09.055>.
- [74] Y. Zhuge, Y.T. Tang, D.G. McCartney, S. Lozano-Perez, R.C. Reed, Characterization of  $\gamma'$  precipitation kinetics in additively manufactured Ni-based superalloy ABD®-900AM, *Metall. Mater. Trans. A* (2026), <https://doi.org/10.1007/s11661-025-08081-z>.
- [75] S.A.J. Forsik, A.D. Dicus, G.A. Colombo, T. Wang, M.E. Epler, E.T. Connolly, J. Srisuriyachot, A.J.G. Lunt, N. Zhou, Influence of the  $\gamma/\gamma'$  misfit on the strain-age cracking resistance of high- $\gamma'$  Ni and CoNi superalloys for additive manufacturing, *Int. Symp. Superalloys*, 2024: pp. 908–917. [doi:10.1007/978-3-031-63937-1\\_84](https://doi.org/10.1007/978-3-031-63937-1_84).
- [76] J.N. Ghoussoub, P. Klupš, W.J.B. Dick-Cleland, K.E. Rankin, S. Utada, P.A.J. Bagot, D.G. McCartney, Y.T. Tang, R.C. Reed, A new class of alumina-forming superalloy for 3D printing, *Addit. Manuf.* 52 (2022) 102608, <https://doi.org/10.1016/j.addma.2022.102608>.
- [77] *Superalloys2024 Additive manufacturing*, *Superalloys2024 Additive manufacturing*. Mineral Metals & Materials Series, Springer Science and Business Media Deutschland GmbH, 2024, pp. 799–810, [https://doi.org/10.1007/978-3-031-63937-1\\_75](https://doi.org/10.1007/978-3-031-63937-1_75).
- [78] H. Wang, K. Han, F. Peng, B. Zhang, Strain-age cracking in vacuum electron beam welded IN738LC alloy during post-weld heat treatment, *Vacuum* 194 (2021) 110588, <https://doi.org/10.1016/j.vacuum.2021.110588>.
- [79] H.E. Evans, H.Y. Li, P. Bowen, A mechanism for stress-aided grain boundary oxidation ahead of cracks, *Scr. Mater.* 69 (2013) 179–182, <https://doi.org/10.1016/j.scriptamat.2013.03.026>.
- [80] H.S. Kitaguchi, H.Y. Li, H.E. Evans, R.G. Ding, I.P. Jones, G. Baxter, P. Bowen, Oxidation ahead of a crack tip in an advanced Ni-based superalloy, *Acta Mater.* 61 (2013) 1968–1981, <https://doi.org/10.1016/j.actamat.2012.12.017>.
- [81] Y.-Q. Hu, H.-Y.H. Zhang, W.-J. Kang, C. Chu, Y.-Q. Hu, H.-Y.H. Zhang, D. Zhang, High temperature oxidation behavior of IN738LC alloy formed by selective laser melting, *J. Mater. Sci.* 57 (2022) 11983–11996, <https://doi.org/10.1007/s10853-022-07345-y>.
- [82] H.T. Mallikarjuna, W.F. Caley, N.L. Richards, Oxidation kinetics and oxide scale characterization of nickel-based superalloy IN738LC at 900°C, *J. Mater. Eng. Perform.* 26 (2017) 4838–4846, <https://doi.org/10.1007/s11665-017-2954-6>.
- [83] J. Wang, H. Xue, Y. Wang, Oxidation behavior of Ni-based superalloy GH738 in static air between 800 and 1000°C, *Rare Met.* 40 (2021) 616–625, <https://doi.org/10.1007/s12598-020-01513-2>.
- [84] A.M. Huntz, Stresses in NiO, Cr<sub>2</sub>O<sub>3</sub> and Al<sub>2</sub>O<sub>3</sub> oxide scales, *Mater. Sci. Eng. A* 201 (1995) 211–228, [https://doi.org/10.1016/0921-5093\(94\)09747-X](https://doi.org/10.1016/0921-5093(94)09747-X).
- [85] H. Springer, D. Raabe, Rapid alloy prototyping: compositional and thermo-mechanical high throughput bulk combinatorial design of structural materials based on the example of 30Mn-1.2C-xAl triplex steels, *Acta Mater.* 60 (2012) 4950–4959, <https://doi.org/10.1016/j.actamat.2012.05.017>.
- [86] D. Zhao, W. Xuan, G. Shao, X. Che, S. Wang, J. Qi, Z. Ren, Unveiling the short-term oxidation behavior of nickel-base superalloy CMSX-4 in high-temperature air, *Corros. Sci.* 251 (2025) 112915, <https://doi.org/10.1016/j.corsci.2025.112915>.
- [87] S. Suresh, G.F. Zamiski, D.R.O. Ritchie, Oxide-induced crack closure: an explanation for near-threshold corrosion fatigue crack growth behavior, *Metall. Trans. A* 12 (1981) 1435–1443, <https://doi.org/10.1007/BF02643688>.
- [88] R.O. Ritchie, Mechanisms of fatigue crack propagation in metals, ceramics and composites: role of crack tip shielding, *Mater. Sci. Eng. A* 103 (1988) 15–28, [https://doi.org/10.1016/0025-5416\(88\)90547-2](https://doi.org/10.1016/0025-5416(88)90547-2).
- [89] L. Chechik, K.A. Christofidou, L. Farquhar, M. Tse, G. Baxter, I. Todd, Tools for the assessment of the laser printability of nickel superalloys, *Metall. Mater. Trans. A* (2023), <https://doi.org/10.1007/s11661-023-07029-5>.
- [90] K. Miao, Z. Ding, R. Li, X. Ji, X. Duan, R. Yao, P. Chen, H. Wu, Mechanisms of heat-treatment-induced cracking in additively manufactured IN738 alloy, *Materials* 16 (2023), <https://doi.org/10.3390/ma16237316>.
- [91] H. Hilal, R. Lancaster, D. Stapleton, G. Baxter, Investigating the influence of process parameters on the structural integrity of an additively manufactured nickel-based superalloy, *Metals* 9 (2019) 1191, <https://doi.org/10.3390/met9111911>.
- [92] S. Ozer, M.N. Doğu, C. Ozdemirel, G.M. Bilgin, M. Gunes, K. Davut, H. Gu, D. Brabazon, Effect of aging treatment on the microstructure, cracking type and crystallographic texture of IN939 fabricated by powder bed fusion-laser beam, *J. Mater. Res. Technol.* 33 (2024) 574–588, <https://doi.org/10.1016/j.jmrt.2024.09.106>.
- [93] H. Yu, J. Liang, Z. Bi, J. Li, W. Xu, Computational design of novel Ni superalloys with low crack susceptibility for additive manufacturing, *Metall. Mater. Trans. A* 53 (2022) 1945–1954, <https://doi.org/10.1007/s11661-022-06653-x>.
- [94] H. Yu, J. Fu, C. Wang, Y. Chen, L. Wang, H. Fang, J. Li, S. van der Zwaag, W. Xu, Robust additive manufacturable Ni superalloys designed by the integrated optimization of local elemental segregation and cracking susceptibility criteria, *Acta Mater.* 266 (2024) 119658, <https://doi.org/10.1016/j.actamat.2024.119658>.
- [95] Z. Liu, Q. Han, Z. Zhang, L. Wang, T. Ma, Z. Gao, B. Song, H. Liu, C. Huang, R. Setchi, Design of a novel crack-free precipitation-strengthened nickel-based superalloy and composites for laser powder bed fusion, *Virtual Phys. Prototyp.* 18 (2023), <https://doi.org/10.1080/17452759.2023.2224769>.
- [96] X. Zhang, Y. Mu, N. Lu, Q. Li, S. Chen, Y. Zhou, X. Sun, J. Liang, J. Li, Effect of solid solution elements on cracking susceptibility of Ni-based superalloys during additive manufacturing, *J. Mater. Sci. Technol.* 190 (2024) 218–228, <https://doi.org/10.1016/j.jmst.2023.11.073>.
- [97] O. Adegoke, J. Andersson, H. Brodin, O. Ojo, R. Pederson, Laser beam powder bed fusion and post processing of alloy 247LC, *Contrib. Pap. MS T19, TMS* (2019) 27–34, [https://doi.org/10.7449/2019/MST\\_2019\\_27\\_34](https://doi.org/10.7449/2019/MST_2019_27_34).